Score-based Enhanced Sampling for Protein Molecular Dynamics

Jiarui Lu [*] [1] [2] Bozitao Zhong [*] [1] [2] Jian Tang [1] [3] [4]

Abstract

The dynamic nature of proteins is crucial for determining their biological functions and properties, and molecular dynamics (MD) simulations stand as a predominant tool to study such phenomena. By utilizing empirically derived force fields, MD simulations explore the conformational space through numerically evolving the system along MD trajectories. However, the high-energy barrier of the force fields can hamper the exploration of MD, resulting in inadequately sampled ensemble. In this paper, we propose leveraging score-based generative models (SGMs) trained on large-scale general protein structures to perform protein conformational sampling to complement traditional MD simulations. Experimental results demonstrate the effectiveness of our approach on several benchmark systems by comparing the results with long MD trajectories and state-of-the-art generative structure prediction models.

1. Introduction

Understanding the dynamical properties of protein is crucial for elucidating the structural mechanism of their biological functions and regulations. Transitions can exist in the conformational ensembles which proteins populate, ranging from angstrom to nanometer in length, and from nanosecond to second in time. Experimental measurements, such as crystallographic B-factors and NMR spectroscopy, can be performed to probe such dynamics. However, these are limited in spatial and temporal scale. Despite the success of structure prediction methods (Baek et al., 2021; Jumper et al., 2021; Lin et al., 2023), which enables the study of proteins based on their high-accuracy structures, the predicted conformational ensembles often lack diversity (Chakravarty & Porter, 2022; Saldaño et al., 2022). Molecular dynamics (MD) serves as a physics-based tool for studying the protein dynamics by employing an empirical force field for simulation. A significant challenge encountered by MD simulations is the high energy-barriers, which forbid transitions within a limited number of simulation steps. Specifically, two typical conformational states with high probability density (low energy) often lie on either side of a high energy barrier. Consequently, transitions between these states can only be achieved with sufficiently long simulation time, otherwise the trajectories remain trapped within the same energy well, resulting in limited exploration.

Over the past decades, enhanced sampling methods have been proposed to overcome the energy barrier and encourage more exploration of MD simulations (Abrams & Bussi, 2013). These methods in general fall into two categories: **(1)** collective variables (CV)-based approaches, such as umbrella sampling (Torrie & Valleau, 1977) and metadynamics (Laio & Parrinello, 2002); **(2)** tempering-based (or CV-free) approaches such as simulated tempering (Marinari & Parisi, 1992) and parallel tempering (synonymous replica exchange molecular dynamics, REMD) (Hansmann, 1997; Sugita & Okamoto, 1999; Swendsen & Wang, 1986), where the term "tempering" refers to methods that involve increasing the temperature of the simulated system to overcome energy barriers (Abrams & Bussi, 2013). The CV-based methods require pre-defined collective variables, or reaction coordinates, which are a low-dimension representation describing the motion of interest using particle coordinates of the system. However, defining proper CV is usually challenging for real systems (Yang et al., 2019). In contrast, tempering-based methods operate by scheduling the system's temperature to facilitate barrier-crossing transitions (Abrams & Bussi, 2013), which borrows the idea from classical simulated annealing approaches for optimization.

Inspired by tempering-based enhanced sampling methods (Marinari & Parisi, 1992), we leverage the score-based generative models (SGMs) (Ho et al., 2020; Sohl-Dickstein et al., 2015; Song et al., 2020) and present the **S**core-based **EN**hanced **S**ampling (**SENS**), a score-based framework for protein conformational sampling which is trained on general protein structures from Protein Data Bank (PDB) (Berman et al., 2000). SENS operates by dispersing the input conformation to its geometric neighborhood and then annealing back the perturbed conformations into respective equilib-

[*] Equal contribution [1] Mila - Québec AI Institute, Montréal, Canada [2] Université de Montréal, Montréal, Canada [3] HEC Montréal, Montréal, Canada [4] CIFAR AI Research Chair. Correspondence to: Jiarui Lu <jiarui.lu@umontreal.ca>, Jian Tang <jian.tang@hec.ca>.

Accepted to ICML 2023 workshop on Structured Probabilistic Inference & Generative Modeling.

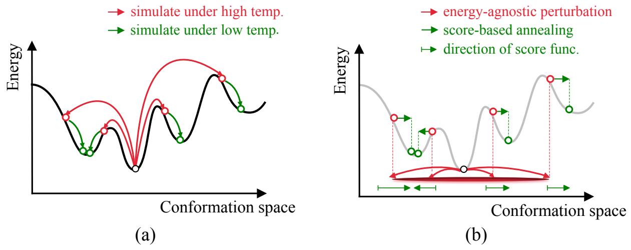

Figure 1. The illustrative comparison between (a) tempering-based enhanced sampling versus (b) sampling via SENS. **(a)** The initial conformations first go through high-temperature MD simulations such that they may "jump out" (red) with large kinetic energy, followed by low-temperature MD steps (green). The motion is highly dependent on the energy surface and hampered by potentially high-energy barrier; **(b)** The initial conformations are randomly dispersed by a perturbation kernel (red). Then the noisy conformations find their respective equilibrium guided by the learned score functions (green). By contrast with (a), these two operations are both energy-agnostic.

rium states with the learned score functions. This approach enables directly sampling of diverse conformation ensembles, thus effectively circumventing the high-energy barrier issue in traditional MD simulations. Moreover, SENS does not rely on any specific simulation data for training, and can be transferred to perform zero-shot conformational sampling by an amortized training. To assess the effectiveness of the SENS, we evaluate it on several benchmark systems, comparing the results with long MD simulations and state-of-the-art generative structure prediction models. The performance of SENS demonstrates its potential as a promising tool for enhanced protein conformational sampling.

2. Preliminary: Score-based generative models

Score-based generative models (SGMs) can be represented by a diffusion process $\mathbf{x}(t) \in \mathbb{R}^d$ defined by the Itô stochastic differential equation(SDE):

$$d\mathbf{x} = \mathbf{f}(\mathbf{x}, t)dt + g(t)d\mathbf{w}, \tag{1}$$

with continuous time index $t \in [0, T]$, where the $\mathbf{f}(\mathbf{x}, t) \in \mathbb{R}^d$ is the time-dependent drift coefficient, $g(t) \in \mathbb{R}$ is the diffusion coefficient, and $\mathbf{w} \in \mathbb{R}^d$ is the standard Wiener process. Then, the corresponding backward SDE that describes the dynamics from $\mathbf{x}(T)$ to $\mathbf{x}(0)$ is (Anderson, 1982; Song et al., 2020):

$$d\mathbf{x} = [\mathbf{f}(\mathbf{x}, t) - g^2(t)\nabla_{\mathbf{x}} \log p_t(\mathbf{x})]dt + g(t)d\mathbf{w}, \tag{2}$$

where dt is negative infinitesimal timestep and $\mathbf{w}$ is the standard Wiener process as continuous time t flows back from T to 0. Two widely used SDE-based schemes (Song et al., 2020) are (1) Variance Exploding (VE) SDE:

$$d\mathbf{x} = \sqrt{\frac{d[\sigma^2(t)]}{dt}}d\mathbf{w}, \tag{3}$$

and (2) Variance Preserving (VP) SDE:

$$d\mathbf{x} = -\frac{1}{2}\beta(t)\mathbf{x}dt + \sqrt{\beta(t)}d\mathbf{w}, \tag{4}$$

where $\sigma(t) \in \mathbb{R}_+$ and $\beta(t) \in \mathbb{R}_+$ are pre-defined noise schedule functions to perturb the data.

3. Score-based enhanced sampling

Suppose we have an observed conformation of a protein (we shall identify it with subscript $[p]$) denoted by $\mathbf{x}_{[p]} \in \mathbb{R}^{3N_{[p]}}$, where $N_{[p]}$ is the total number of atoms of interest. Our goal is to obtain a diverse conformation ensemble $\tilde{\mathbf{X}}^*_{[p]} = \{\tilde{\mathbf{x}}^{(i)}_{[p]}\}$ (members indexed by $i \in \Lambda$) that well captures the dynamics of p with $\mathbf{x}_{[p]}$ as starting point. To achieve this, consider two stochastic operators: (1) *heat* operator $\mathbf{H}_\epsilon : \mathbb{R}^{3N_{[p]} \times |\Lambda|} \rightarrow \mathbb{R}^{3N_{[p]} \times |\Lambda|}$. and (2) *anneal* operator $\mathbf{A}_\eta : \mathbb{R}^{3N_{[p]} \times |\Lambda|} \rightarrow \mathbb{R}^{3N_{[p]} \times |\Lambda|}$, where ϵ, η are random variables governing the randomness, and $|\Lambda|$ is the size of ensemble to be sampled. Inspired by tempering based enhanced sampling (Hansmann, 1997; Marinari & Parisi, 1992; Sugita & Okamoto, 1999; Swendsen & Wang, 1986), the problem can be described as follows:

$$\tilde{\mathbf{X}}_{[p]} = \mathbf{A}_\eta(\mathbf{H}_\epsilon(\mathbf{X}_{[p]})), \tag{5}$$

where $\mathbf{X}_{[p]} = \text{repeat}(\mathbf{x}_{[p]}; |\Lambda|) \in \mathbb{R}^{3N_{[p]} \times |\Lambda|}$ is an operation that repeats $\mathbf{x}_{[p]}$ for $|\Lambda|$ times to create a set of replicas before simulation. The above formulation indicates that the conformational ensemble can be obtained as a composition of *heat* and *anneal* operators. For simplicity, we consider independent operators such that Eq. (5) can be replaced by its point-to-point versions, which are adopted in later paragraphs.

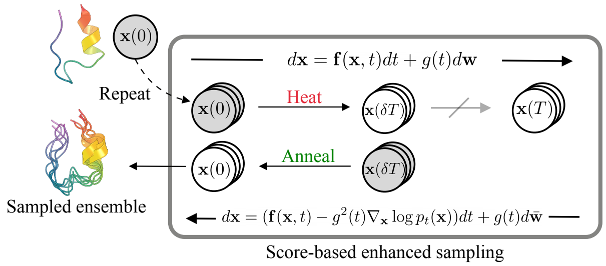
x(0)
Repeat
$d\mathbf{x} = \mathbf{f}(\mathbf{x}, t)dt + g(t)d\mathbf{w}$
x(0)
Heat
x(δT)
x(T)
Sampled ensemble
x(0)
Anneal
x(δT)
$d\mathbf{x} = (\mathbf{f}(\mathbf{x}, t) - g^2(t)\nabla_{\mathbf{x}} \log p_t(\mathbf{x}))dt + g(t)d\bar{\mathbf{w}}$
Score-based enhanced sampling

Figure 2. Illustration of SENS. Given an initial conformation (Trp-cage as example, PDB ID: 2JOF), a number of replicas are created (repeat) and fed to the *heat* process. The *heat* process respectively perturbs each replica until a specific time δT, where δ $(0 < \delta < 1)$ is a parameter controlling the range of perturbation. Afterwards, the *anneal* process yields the sampled ensemble.

Based on this, we propose a novel score-based framework that realizes these two operators. We reason that, as a generative model: (1) The perturbing-denoising nature of SGMs transforms the input within the same space; (2) The continuous diffusion process allows us to partially perturb the input instead of projecting into a latent space; (3) SGMs have proved their effectiveness for modeling multimodal distribution (Dhariwal & Nichol, 2021) and are seldom haunted by the mode collapse issue.

3.1. Sampling via forward-backward dynamics

To better sample protein conformational ensembles, we propose a forward-backward dynamics that leverages the multi-level score functions learned by score matching. Firstly, consider the following realization of operators defined by integrals, given $\delta \in (0,1)$ is the parameter controlling the perturbation scale:

$$\mathbf{H}_{\mathbf{w}}(\mathbf{x}(0)) := \mathbf{x}(0) + \int_0^{\delta T} \left[\mathbf{f}(\mathbf{x}(t),t)dt + g(t)d\mathbf{w}\right], \quad (6)$$

where $\mathbf{x}(t)$ is the diffusion process as Eq. (1), with initial value $\mathbf{x}(0)$ being input geometry as in classical MD simulations. The $\mathbf{f}(\cdot,\cdot), g(\cdot)$ and $\mathbf{w} = \mathbf{w}(t)$ are defined over time domain $t \in [0,T]$ according to Eq. (1). And with positive dt:

$$\mathbf{A}_{\bar{\mathbf{w}}}(\mathbf{x}(\delta T)) := \mathbf{x}(\delta T) + \int_{\delta T}^{2\delta T} g(\tau(t))d\bar{\mathbf{w}}$$
$$+ \int_{\delta T}^{2\delta T} \left[-\mathbf{f}(\bar{\mathbf{x}}(t),\tau(t)) + g^2(\tau(t))\nabla_{\bar{\mathbf{x}}(t)} \log p_t(\bar{\mathbf{x}}(t))\right] dt, \quad (7)$$

where $\tau(t) := 2\delta T - t$ for brief notation. $\bar{\mathbf{x}}(t) := \mathbf{x}(2\delta T - t)$, $\bar{\mathbf{w}} := \mathbf{w}(2\delta T - t)$ are identical processes as Eq. (1) and (2) with change of variable; the rest of symbols are denoted the same as above. Then, the sampled conformation $\tilde{\mathbf{x}}$ by the forward-backward dynamics take the following form by composing two operators:

$$\tilde{\mathbf{x}} = \mathbf{A}_{\bar{\mathbf{w}}}(\mathbf{H}_{\mathbf{w}}(\mathbf{x}(0))) \quad (8)$$

Intuitively, Eq. (8) is composed of both forward and backward SDEs (Eq. (1) and (2)), first enforcing proper perturbation and then mapping the perturbed examples into the annealed conformations. The definitions above realize the *heat* and *anneal* operator respectively by pushing forward a new SDE from $t = 0$ to $2\delta T$.

3.2. Score matching objective

To approximate the score functions in Eq. (8), we can train a time-dependent score network $\mathbf{s}_\theta(\mathbf{x},t)$ via the following objectives:

$$\arg\min_\theta \mathbb{E}_t \left\{\lambda(t)\mathbb{E}_{\mathbf{x}_0,\mathbf{x}_t}\left[\|\mathbf{s}_\theta(\mathbf{x}_t,t) - \nabla_{\mathbf{x}_t} \log p_{t|0}(\mathbf{x}_t|\mathbf{x}_0)\|^2\right]\right\}, \quad (9)$$

where $\lambda(t) > 0$ is a positive loss reweighting function, $\mathbf{x}_t \sim p_{t|0}(\mathbf{x}_t|\mathbf{x}_0)$ and $\mathbf{x}_0 \sim p(\mathbf{x})$ are defined by the corresponding perturbation kernel, and the time t is uniformly sampled over cropped time domain $[0, t_m]$ ($\delta T \le t_m \le T$ is the pre-specified upper bound of δT used during inference).

3.3. Control sampling with temperature

Temperature plays an important role during sampling by effectively trade-off diversity and fidelity (i.e. exploration and exploitation). Given a probability density $p(\mathbf{x})$, the tempering distribution by an inverse temperature factor $\beta > 0$ is denoted as $p^{(\beta)}(\mathbf{x}) = (p(\mathbf{x}))^\beta / Z_\beta$, where Z_β is the normalizing constant $\int_{\mathbf{x}} (p(\mathbf{x}))^\beta d\mathbf{x}$, which only depends on β. The tempering strategy is commonly used for categorical distributions, such as language modeling, via rescaling the logits. Unfortunately, for SGMs, the temperature coefficient does not explicitly appear in the backward SDE. In this work, we propose using an β-related affine transformation on the score function $\nabla_{\mathbf{x}} \log p_t(\mathbf{x})$ to achieve low-temperature sampling. Details can be found in appendix.

3.4. Model architectures

To parameterize the score network $s_\theta(\mathbf{x},t)$ for conformation sampling, we adopt the modified EGNN (Satorras et al., 2021) with SE(3)-equivariant property. Following (Janson et al., 2023; Jing et al., 2023), we focus on residue-level protein structures, where the representation of conformation is denoted as $\mathbf{x} = (x_1, x_2, \ldots, x_N) \in \mathbb{R}^{N\times 3}$, where $x_i \in \mathbb{R}^3$ is the coordinate of C_α atom of the i's residue. For message passing, we construct a k-nearest-neighbors (kNN) graph with maximum number of neighbors set to $k = 64$. To attend to the chain structure of protein, sinusoidal positional embedding (Vaswani et al., 2017) is appended to the node feature along with the time embedding, which is used to condition the score network. See appendix for the detailed model implementations.

4. Experiment

To assess the performance of SENS on zero-shot conformational sampling, we set up the benchmark set consisting of 12 fast-folding proteins with up to 1ms all-atom MD trajectories as reference (named *reference* MD) (Lindorff-Larsen et al., 2011). Specifically, they include Chignolin, Trp-cage, BBA, Villin, WW domain, NTL9, BBL, Protein B, Homeodomain, Protein G, α3D and λ-repressor. We generate 100 conformations for each target from SENS and baseline models. The conformations from reference MD are uniformly sampled from MD trajectories in the same size with different timescales: 1μs, 10μs, full (the longest time in data). For example, 10μs means conformations are sampled from trajectories with the first 10μs. To better show the effect of temperature in MD simulation, we run two independent 0.1μs simulations (named *short* MD) with different temperatures for comparison as well.

Table 1. Benchmark results of different methods with MD references. The samples from reference MD trajectories are colored as brown while samples from other baselines are obtained by running their codes. The cell color indicates the top three best scores in each column, and the best result of our methods are **bolded**.

	Validity(↑)	JS-D(↓)	JS-Rg (↓)	Div-TM(↑)	Div-RMSD(↑)
AF2 *reducedMSA* (Vani et al., 2023)	1.000	0.330	0.517	0.057	0.049
AF2 *noMSA*	0.995	0.321	0.431	0.194	0.224
EigenFold (Jing et al., 2023)	0.894	0.249	0.477	0.218	0.166
idpGAN (Janson et al., 2023)	1.000	0.251	0.530	0.839	1.346
SENS ($\delta = 0.3, \beta = 5.0$)	**1.000**	0.283	0.524	0.543	0.275
SENS ($\delta = 0.4, \beta = 5.0$)	**1.000**	0.252	0.422	0.647	0.401
SENS ($\delta = 0.3, \beta = 2.0$)	**1.000**	0.267	0.474	0.536	0.277
SENS ($\delta = 0.4, \beta = 2.0$)	0.998	0.217	0.401	0.693	0.440
SENS ($\delta = 0.3, \beta = 1.0$)	0.998	0.257	0.416	0.576	0.295
SENS ($\delta = 0.4, \beta = 1.0$)	0.993	**0.203**	**0.338**	**0.734**	**0.498**
Short MD 0.1μs	1.000	0.217	0.300	0.508	0.449
Short MD 0.1μs (high temp.)	1.000	0.204	0.285	0.536	0.495
Reference 1μs (Lindorff-Larsen et al., 2011)	1.000	0.135	0.178	0.582	0.642
Reference 10μs (Lindorff-Larsen et al., 2011)	1.000	0.100	0.156	0.650	0.736
Reference full (Lindorff-Larsen et al., 2011)	1.000	0.000	0.000	0.659	0.756

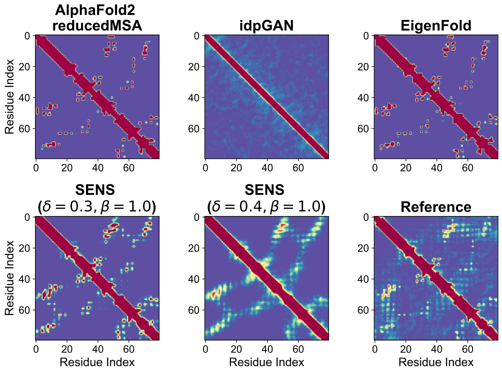

Figure 3. Contact probability distribution for protein *Lambda* (PDB ID: 1LMB) conformations from different methods.

The training and validation examples for training SENS are acquired from PDB. We adopted the VESDE diffusion as backbone model for SENS. Baseline models were selected as (1) AlphaFold2 (AF2) (Jumper et al., 2021) with either no MSA (sequence only) or reduced MSA (Chakravarty & Porter, 2022) as input; (2) idpGAN (Janson et al., 2023), a recently reported conditional generative method based on generative adversarial networks (GAN); (3) EigenFold (Jing et al., 2023), a recently developed generative structure prediction model that employs harmonic diffusion to enable diversity. More details of data and baselines will be listed in the appendix.

Our evaluation metrics are categorized into: **Validity** is defined by clash ratio which is the number of clash-free samples divided by the number of samples. Clash is counted by examining whether a contact pair is within certain distance threshold. **Fidelity** compares the distribution divergence between sampled conformations and the full reference MD. We use the symmetric Jensen-Shannon (JS) divergence based on (i) pairwise distance distribution (JS-D) and (ii) radius of gyration distribution (JS-Rg) as in idpGAN (Janson et al., 2023). **Diversity** is defined the average pairwise dissimilarity scores based on root mean square deviation (RMSD, unit: nm) and TM-score (Zhang & Skolnick, 2004) for the generated ensemble. For the latter, we apply the inverse TMscore ($1 - \text{TM}(i, j)$) to express "diversity" together with RMSD. During evaluation, each metric was averaged among different benchmark targets to give the finally evaluation. As shown in Table 1, SENS's performance validated its effectiveness in sampling diverse, yet physically plausible conformations when compared to other (generative) structure prediction models and traditional MD simulations. All structure generation models suffered from limited diversity and bad fidelity. Though idpGAN showed outstanding sampling diversity, its conformations tend to be disordered and deviate from true distribution (also as shown in Fig. 3). Notably for SENS, increasing temperature (w/ declined β) results in more diverse ensembles and better coverage of reference conformation space by trading off a bit validity. The detailed of metrics and results can be found in appendix.

To better demonstrate the performance of our proposed method, we conducted a case study using the bovine pancreatic trypsin inhibitor (BPTI) protein. The dynamic properties of BPTI have been extensively studied using long molecular dynamics (MD) simulations (Shaw et al., 2010). Experiments and MD simulations revealed BPTI exhibits five distinct structural clusters (Shaw et al., 2010). Similar to our benchmark, full MD trajectory (1,013 μs) were used as reference and generative structure prediction methods were compared with ours. Principal Component Analysis (PCA) were employed for dimension reduction to illustrate the conformation distribution. As shown in the upper panel of Fig. 4, AlphaFold2 redusedMSA and EigenFold were

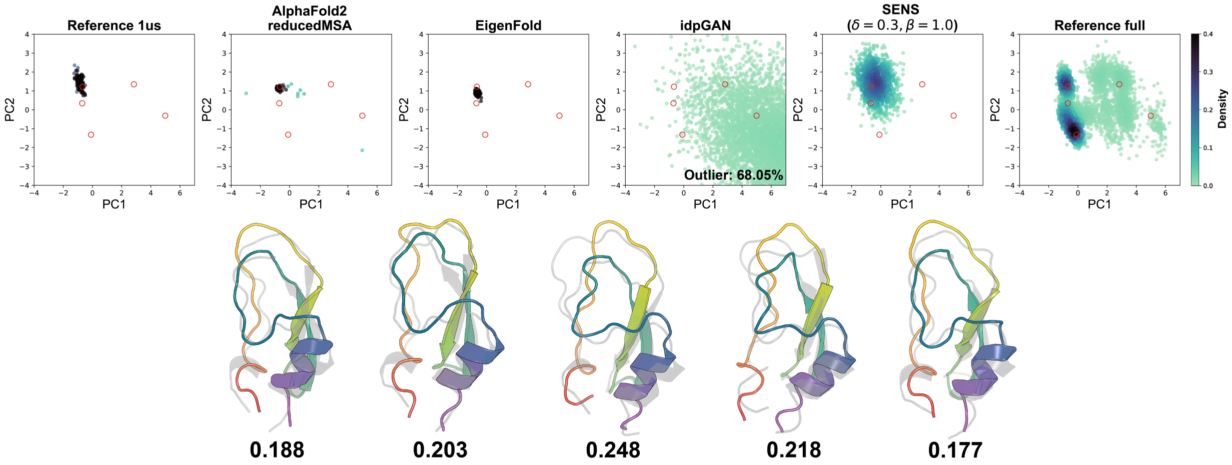

Figure 4. Visualization of sampled BPTI conformations and structure clusters. The upper panel illustrates a PCA-reduced map of the sampled conformations, pairwise distances were used as features. The color gradient represents the estimated density. Red circles indicate the locations of five structure clusters. 68.05% of the idpGAN samples are found outside the depicted area. The lower panel depicts the nearest sampled structure of SENS($\delta = 0.3, \beta = 1.0$, colored) to the five structure clusters (grey). RMSD (nm) is presented below.

only able to sample a constrained region, while idpGAN sampled an excessive amount of disordered conformations, which are unsuitable for structured proteins like BPTI. In contrast, our method was able to sample a reasonable and diverse range of conformations, outperform 1μs simulations, and approaching the full reference trajectory. In the lower panel of Fig. 4, we present the nearest sampled structure from SENS($\delta = 0.3, \beta = 1.0$, colored) to the five structural clusters. Similar structure can be found for all five structure clusters within RMSD 0.25 nm. These findings demonstrates a promising performance for SENS in generating reliable and diverse protein conformations.

5. Conclusion

In this paper, we presented SENS, a score-based framework for protein conformational sampling inspired by tempering-based enhanced sampling methods in molecular dynamics (MD) simulations. SENS firstly disperses the initial conformation within its neighborhood, followed by a score-based annealing process. We trained SENS on general protein structure data from the Protein Data Bank (PDB) using score matching objectives. Experimental results on several MD benchmarking systems demonstrate that SENS can effectively sample a diverse ensemble from the initial conformation and achieve comparable performance with long simulation results.

Limitations of SENS and potential future directions encompass several aspects: **(1)** The isotropic perturbation kernels could be improved by incorporating drift and diffusion terms specifically designed for protein structures (Ingraham et al., 2022; Jing et al., 2023). This modification would allow the perturbations based on non-Euclidean coordinates, drawing parallels to CV-based enhanced sampling techniques. **(2)** SENS has mainly been tested on VE/VPSDE diffusion (Song et al., 2020) as proof of concept. The backward process, however, can be computationally intensive due to plenty of network evaluations. To accelerate SENS for efficient sampling, one might consider the use of distillation (Salimans & Ho, 2022) or more advanced frameworks such as consistency models (Song et al., 2023). **(3)** An interesting application of SENS is to plug it in atom-level MD simulations by providing out-of-barrier conformation set as MD starting points. To achieve this, one may either extend SENS for modeling all-atom structures, or develop backmapping algorithms like in (Yang & Gómez-Bombarelli, 2023). **(4)** The proposed method, in its current form, relies solely on structure data for training. As amino acid sequences was also reported to be used for inferring protein structure (Lin et al., 2023), it's worth exploring the feasibility to use sequence as conditional signal when modeling dynamics. For example, one can provide gradient guidance during the backward SDE (Song et al., 2020) using an external classifier, which could be trained on sequence-structure pairing data using a CLIP-like architecture (Radford et al., 2021).

References

Abrams, C. and Bussi, G. Enhanced sampling in molecular dynamics using metadynamics, replica-exchange, and temperature-acceleration. *Entropy*, 16(1):163–199, 2013.

Anand, N. and Achim, T. Protein structure and sequence generation with equivariant denoising diffusion probabilistic models. *arXiv preprint arXiv:2205.15019*, 2022.

Anderson, B. D. Reverse-time diffusion equation models. *Stochastic Processes and their Applications*, 12(3):313–326, 1982.

Arts, M., Satorras, V. G., Huang, C.-W., Zuegner, D., Federici, M., Clementi, C., Noé, F., Pinsler, R., and Berg, R. v. d. Two for one: Diffusion models and force fields for coarse-grained molecular dynamics. *arXiv preprint arXiv:2302.00600*, 2023.

Baek, M., DiMaio, F., Anishchenko, I., Dauparas, J., Ovchinnikov, S., Lee, G. R., Wang, J., Cong, Q., Kinch, L. N., Schaeffer, R. D., et al. Accurate prediction of protein structures and interactions using a three-track neural network. *Science*, 373(6557):871–876, 2021.

Belanger, D. and McCallum, A. Structured prediction energy networks. In *International Conference on Machine Learning*, pp. 983–992. PMLR, 2016.

Berman, H. M., Westbrook, J., Feng, Z., Gilliland, G., Bhat, T. N., Weissig, H., Shindyalov, I. N., and Bourne, P. E. The protein data bank. *Nucleic acids research*, 28(1): 235–242, 2000.

Bernardi, R. C., Melo, M. C., and Schulten, K. Enhanced sampling techniques in molecular dynamics simulations of biological systems. *Biochimica et Biophysica Acta (BBA)-General Subjects*, 1850(5):872–877, 2015.

Bishop, C. M. and Nasrabadi, N. M. *Pattern recognition and machine learning*, volume 4. Springer, 2006.

Cao, L., Goreshnik, I., Coventry, B., Case, J. B., Miller, L., Kozodoy, L., Chen, R. E., Carter, L., Walls, A. C., Park, Y.-J., et al. De novo design of picomolar sars-cov-2 miniprotein inhibitors. *Science*, 370(6515):426–431, 2020.

Chakravarty, D. and Porter, L. L. Alphafold2 fails to predict protein fold switching. *Protein Science*, 31(6):e4353, 2022.

Chen, R. T., Rubanova, Y., Bettencourt, J., and Duvenaud, D. K. Neural ordinary differential equations. *Advances in neural information processing systems*, 31, 2018.

Ciccotti, G. and Ryckaert, J.-P. Molecular dynamics simulation of rigid molecules. *Computer Physics Reports*, 4(6): 346–392, 1986.

Corso, G., Stärk, H., Jing, B., Barzilay, R., and Jaakkola, T. Diffdock: Diffusion steps, twists, and turns for molecular docking. *arXiv preprint arXiv:2210.01776*, 2022.

Darden, T., York, D., and Pedersen, L. Particle mesh ewald: An n log (n) method for ewald sums in large systems. *The Journal of chemical physics*, 98(12):10089–10092, 1993.

Dauparas, J., Anishchenko, I., Bennett, N., Bai, H., Ragotte, R. J., Milles, L. F., Wicky, B. I., Courbet, A., de Haas, R. J., Bethel, N., et al. Robust deep learning–based protein sequence design using proteinmpnn. *Science*, 378 (6615):49–56, 2022.

Del Alamo, D., Sala, D., Mchaourab, H. S., and Meiler, J. Sampling alternative conformational states of transporters and receptors with alphafold2. *Elife*, 11:e75751, 2022.

Dhariwal, P. and Nichol, A. Diffusion models beat gans on image synthesis. *Advances in Neural Information Processing Systems*, 34:8780–8794, 2021.

Dinh, L., Krueger, D., and Bengio, Y. Nice: Non-linear independent components estimation. *arXiv preprint arXiv:1410.8516*, 2014.

Eastman, P., Swails, J., Chodera, J. D., McGibbon, R. T., Zhao, Y., Beauchamp, K. A., Wang, L.-P., Simmonett, A. C., Harrigan, M. P., Stern, C. D., et al. Openmm 7: Rapid development of high performance algorithms for molecular dynamics. *PLoS computational biology*, 13(7): e1005659, 2017.

Fuchs, F., Worrall, D., Fischer, V., and Welling, M. Se (3)-transformers: 3d roto-translation equivariant attention networks. *Advances in Neural Information Processing Systems*, 33:1970–1981, 2020.

Grathwohl, W., Chen, R. T., Bettencourt, J., Sutskever, I., and Duvenaud, D. Ffjord: Free-form continuous dynamics for scalable reversible generative models. *arXiv preprint arXiv:1810.01367*, 2018.

Hansmann, U. H. Parallel tempering algorithm for conformational studies of biological molecules. *Chemical Physics Letters*, 281(1-3):140–150, 1997.

Heusel, M., Ramsauer, H., Unterthiner, T., Nessler, B., and Hochreiter, S. Gans trained by a two time-scale update rule converge to a local nash equilibrium. *Advances in neural information processing systems*, 30, 2017.

Ho, J., Jain, A., and Abbeel, P. Denoising diffusion probabilistic models. *Advances in Neural Information Processing Systems*, 33:6840–6851, 2020.

Hutchinson, M. F. A stochastic estimator of the trace of the influence matrix for laplacian smoothing splines. *Communications in Statistics-Simulation and Computation*, 18(3):1059–1076, 1989.

Ingraham, J., Baranov, M., Costello, Z., Frappier, V., Ismail, A., Tie, S., Wang, W., Xue, V., Obermeyer, F., Beam, A., et al. Illuminating protein space with a programmable generative model. *bioRxiv*, pp. 2022–12, 2022.

Janson, G., Valdes-Garcia, G., Heo, L., and Feig, M. Direct generation of protein conformational ensembles via machine learning. *Nature Communications*, 14(1):774, 2023.

Jing, B., Erives, E., Pao-Huang, P., Corso, G., Berger, B., and Jaakkola, T. Eigenfold: Generative protein structure prediction with diffusion models. *arXiv preprint arXiv:2304.02198*, 2023.

Jumper, J., Evans, R., Pritzel, A., Green, T., Figurnov, M., Ronneberger, O., Tunyasuvunakool, K., Bates, R., Žídek, A., Potapenko, A., et al. Highly accurate protein structure prediction with alphafold. *Nature*, 596(7873):583–589, 2021.

Karplus, M. and McCammon, J. A. Molecular dynamics simulations of biomolecules. *Nature structural biology*, 9(9):646–652, 2002.

Kohler, J., Chen, Y., Kramer, A., Clementi, C., and Noé, F. Flow-matching: Efficient coarse-graining of molecular dynamics without forces. *Journal of Chemical Theory and Computation*, 19(3):942–952, 2023.

Laio, A. and Parrinello, M. Escaping free-energy minima. *Proceedings of the national academy of sciences*, 99(20): 12562–12566, 2002.

Lin, Y. and AlQuraishi, M. Generating novel, designable, and diverse protein structures by equivariantly diffusing oriented residue clouds. *arXiv preprint arXiv:2301.12485*, 2023.

Lin, Z., Akin, H., Rao, R., Hie, B., Zhu, Z., Lu, W., Smetanin, N., Verkuil, R., Kabeli, O., Shmueli, Y., et al. Evolutionary-scale prediction of atomic-level protein structure with a language model. *Science*, 379(6637): 1123–1130, 2023.

Lindorff-Larsen, K., Piana, S., Dror, R. O., and Shaw, D. E. How fast-folding proteins fold. *Science*, 334(6055):517–520, 2011.

Luo, S., Su, Y., Peng, X., Wang, S., Peng, J., and Ma, J. Antigen-specific antibody design and optimization with diffusion-based generative models. *bioRxiv*, pp. 2022–07, 2022.

Maier, J. A., Martinez, C., Kasavajhala, K., Wickstrom, L., Hauser, K. E., and Simmerling, C. ff14sb: improving the accuracy of protein side chain and backbone parameters from ff99sb. *Journal of chemical theory and computation*, 11(8):3696–3713, 2015.

Marinari, E. and Parisi, G. Simulated tempering: a new monte carlo scheme. *Europhysics letters*, 19(6):451, 1992.

Noé, F., Olsson, S., Köhler, J., and Wu, H. Boltzmann generators: Sampling equilibrium states of many-body systems with deep learning. *Science*, 365(6457):eaaw1147, 2019.

Radford, A., Kim, J. W., Hallacy, C., Ramesh, A., Goh, G., Agarwal, S., Sastry, G., Askell, A., Mishkin, P., Clark, J., et al. Learning transferable visual models from natural language supervision. In *International conference on machine learning*, pp. 8748–8763. PMLR, 2021.

Ramachandran, S., Kota, P., Ding, F., and Dokholyan, N. V. Automated minimization of steric clashes in protein structures. *Proteins: Structure, Function, and Bioinformatics*, 79(1):261–270, 2011.

Rezende, D. and Mohamed, S. Variational inference with normalizing flows. In *International conference on machine learning*, pp. 1530–1538. PMLR, 2015.

Roweis, S. and Ghahramani, Z. A unifying review of linear gaussian models. *Neural computation*, 11(2):305–345, 1999.

Ryckaert, J.-P., Ciccotti, G., and Berendsen, H. J. Numerical integration of the cartesian equations of motion of a system with constraints: molecular dynamics of n-alkanes. *Journal of computational physics*, 23(3):327–341, 1977.

Saldaño, T., Escobedo, N., Marchetti, J., Zea, D. J., Mac Donagh, J., Velez Rueda, A. J., Gonik, E., García Melani, A., Novomisky Nechcoff, J., Salas, M. N., et al. Impact of protein conformational diversity on alphafold predictions. *Bioinformatics*, 38(10):2742–2748, 2022.

Salimans, T. and Ho, J. Progressive distillation for fast sampling of diffusion models. *arXiv preprint arXiv:2202.00512*, 2022.

Satorras, V. G., Hoogeboom, E., and Welling, M. E (n) equivariant graph neural networks. In *International conference on machine learning*, pp. 9323–9332. PMLR, 2021.

Shaw, D. E., Maragakis, P., Lindorff-Larsen, K., Piana, S., Dror, R. O., Eastwood, M. P., Bank, J. A., Jumper, J. M., Salmon, J. K., Shan, Y., et al. Atomic-level characterization of the structural dynamics of proteins. *Science*, 330 (6002):341–346, 2010.

Shi, C., Wang, C., Lu, J., Zhong, B., and Tang, J. Protein sequence and structure co-design with equivariant translation. *arXiv preprint arXiv:2210.08761*, 2022.

Sillitoe, I., Bordin, N., Dawson, N., Waman, V. P., Ashford, P., Scholes, H. M., Pang, C. S., Woodridge, L., Rauer, C., Sen, N., et al. Cath: increased structural coverage of functional space. *Nucleic acids research*, 49(D1):D266–D273, 2021.

Skilling, J. The eigenvalues of mega-dimensional matrices. *Maximum Entropy and Bayesian Methods: Cambridge, England, 1988*, pp. 455–466, 1989.

Sohl-Dickstein, J., Weiss, E., Maheswaranathan, N., and Ganguli, S. Deep unsupervised learning using nonequilibrium thermodynamics. In *International Conference on Machine Learning*, pp. 2256–2265. PMLR, 2015.

Song, Y., Sohl-Dickstein, J., Kingma, D. P., Kumar, A., Ermon, S., and Poole, B. Score-based generative modeling through stochastic differential equations. *arXiv preprint arXiv:2011.13456*, 2020.

Song, Y., Dhariwal, P., Chen, M., and Sutskever, I. Consistency models. *arXiv preprint arXiv:2303.01469*, 2023.

Sugita, Y. and Okamoto, Y. Replica-exchange molecular dynamics method for protein folding. *Chemical physics letters*, 314(1-2):141–151, 1999.

Swendsen, R. H. and Wang, J.-S. Replica monte carlo simulation of spin-glasses. *Physical review letters*, 57 (21):2607, 1986.

Thomas, N., Smidt, T., Kearnes, S., Yang, L., Li, L., Kohlhoff, K., and Riley, P. Tensor field networks: Rotation-and translation-equivariant neural networks for 3d point clouds. *arXiv preprint arXiv:1802.08219*, 2018.

Torrie, G. M. and Valleau, J. P. Nonphysical sampling distributions in monte carlo free-energy estimation: Umbrella sampling. *Journal of Computational Physics*, 23 (2):187–199, 1977.

Trippe, B. L., Yim, J., Tischer, D., Broderick, T., Baker, D., Barzilay, R., and Jaakkola, T. Diffusion probabilistic modeling of protein backbones in 3d for the motif-scaffolding problem. *arXiv preprint arXiv:2206.04119*, 2022.

Vani, B. P., Aranganathan, A., Wang, D., and Tiwary, P. From sequence to boltzmann weighted ensemble of structures with alphafold2-rave. *bioRxiv*, pp. 2022–05, 2022.

Vani, B. P., Aranganathan, A., Wang, D., and Tiwary, P. Alphafold2-rave: From sequence to boltzmann ranking. *Journal of Chemical Theory and Computation*, 2023.

Vaswani, A., Shazeer, N., Parmar, N., Uszkoreit, J., Jones, L., Gomez, A. N., Kaiser, Ł., and Polosukhin, I. Attention is all you need. *Advances in neural information processing systems*, 30, 2017.

Wang, J., Olsson, S., Wehmeyer, C., Pérez, A., Charron, N. E., De Fabritiis, G., Noé, F., and Clementi, C. Machine learning of coarse-grained molecular dynamics force fields. *ACS central science*, 5(5):755–767, 2019.

Watson, J. L., Juergens, D., Bennett, N. R., Trippe, B. L., Yim, J., Eisenach, H. E., Ahern, W., Borst, A. J., Ragotte, R. J., Milles, L. F., et al. Broadly applicable and accurate protein design by integrating structure prediction networks and diffusion generative models. *bioRxiv*, pp. 2022–12, 2022.

Wayment-Steele, H. K., Ovchinnikov, S., Colwell, L., and Kern, D. Prediction of multiple conformational states by combining sequence clustering with alphafold2. *bioRxiv*, pp. 2022–10, 2022.

Wu, K. E., Yang, K. K., Berg, R. v. d., Zou, J. Y., Lu, A. X., and Amini, A. P. Protein structure generation via folding diffusion. *arXiv preprint arXiv:2209.15611*, 2022a.

Wu, R., Ding, F., Wang, R., Shen, R., Zhang, X., Luo, S., Su, C., Wu, Z., Xie, Q., Berger, B., et al. High-resolution de novo structure prediction from primary sequence. *BioRxiv*, pp. 2022–07, 2022b.

Yang, S. and Gómez-Bombarelli, R. Chemically transferable generative backmapping of coarse-grained proteins. *arXiv preprint arXiv:2303.01569*, 2023.

Yang, Y. I., Shao, Q., Zhang, J., Yang, L., and Gao, Y. Q. Enhanced sampling in molecular dynamics. *The Journal of chemical physics*, 151(7):070902, 2019.

Yim, J., Trippe, B. L., De Bortoli, V., Mathieu, E., Doucet, A., Barzilay, R., and Jaakkola, T. Se (3) diffusion model with application to protein backbone generation. *arXiv preprint arXiv:2302.02277*, 2023.

Zhang, Y. and Skolnick, J. Scoring function for automated assessment of protein structure template quality. *Proteins: Structure, Function, and Bioinformatics*, 57(4):702–710, 2004.

Zhong, B., Su, X., Wen, M., Zuo, S., Hong, L., and Lin, J. Parafold: paralleling alphafold for large-scale predictions. In *International Conference on High Performance Computing in Asia-Pacific Region Workshops*, pp. 1–9, 2022.

A. Further details of SENS

A.1. Equivariant score network

In this section, we elaborate the equivariant model architecture used to parameterize the score function for SENS. Basically, we adopt the E(n)-equivariant graph neural networks (EGNN) (Satorras et al., 2021) given its simple and computationally efficient form, with an additional SE(3)-equivariant convolutional layer to achieve the SE(3)-equivariant property during the backward process. The SE(3)-equivariant property of a function $(\boldsymbol{x}', \boldsymbol{h}') = \boldsymbol{f}(\boldsymbol{x}, \boldsymbol{h})$ with respect to group transformations operating on three-dimensional (3D) coordinates $\boldsymbol{x} \in \mathbb{R}^{N\times 3}$ and hidden features $\boldsymbol{h} \in \mathbb{R}^{N\times d}$, is defined below:

$$(\boldsymbol{x}'\boldsymbol{R}^\top + \boldsymbol{t}, \boldsymbol{h}') = \boldsymbol{f}(\boldsymbol{x}\boldsymbol{R}^\top + \boldsymbol{t}, \boldsymbol{h}), \tag{10}$$

where rotation matrix $\boldsymbol{R} \in \mathbb{R}^{3\times 3}$ (orthogonal with determinant 1) and translation vector $\boldsymbol{t} \in \mathbb{R}^3$ define the special Euclidean group (SE(3) group) transformations, where any rotation (yet not reflection) and translation in 3D space are included. The hidden features are invariant to the group actions and thus not affected by the transformation. The advantage of leveraging such equivariance is that the conformations generated via a group orbit, i.e., by applying all group actions on some specific input $\boldsymbol{x}$, can be equivalent (trivial) in 3D space because they belong to the same molecular species. Neural networks equipped with equivariant property can focus more on performing non-trivial mapping for the conformations.

The SE(3) convolutional layer is applied before the EGNN network, and adopts the definition in SE(3)-transformer (Fuchs et al., 2020) and tensor field networks (TFN) (Thomas et al., 2018). To simplify, we only consider up to type-1 features (scalar and vector field) from each node's neighborhood for the convolution, which means, the output type-l ($l = 0, 1$) feature for node i is:

$$\boldsymbol{f}^l_{\text{out},i} = w^{ll}\boldsymbol{f}^l_{\text{in},i} + \sum_{k=0}^{1}\sum_{j\in\mathcal{N}_i} \boldsymbol{W}^{lk}(\boldsymbol{x}_j - \boldsymbol{x}_i)\boldsymbol{f}^k_{\text{in},j}, \tag{11}$$

where $\boldsymbol{f}^l_{\text{in},i}$ is the type-l feature for node i, $\boldsymbol{W}^{lk} : \mathbb{R}^3 \to \mathbb{R}^{(2l+1)\times(2k+1)}$ is the learnable kernel mapping from type-k features to type-l features, and $w^{ll}\boldsymbol{f}^l_{\text{in},i}$ is the self-interaction term with learnable parameters $w^{ll} \in \mathbb{R}$. As shown in (Thomas et al., 2018), such kernel is a combination of equivariant basis kernels $\{\boldsymbol{W}^{lk}_J\}^{k+l}_{J=|k-l|}$, or formally

$$\boldsymbol{W}^{lk}(\boldsymbol{x}) = \sum_{J=|k-l|}^{k+l} \phi^{lk}_J(\|\boldsymbol{x}\|)\boldsymbol{W}^{lk}_J(\boldsymbol{x}), \text{ where } \boldsymbol{W}^{lk}_J(\boldsymbol{x}) = \sum_{m=-J}^{J} Y_{Jm}(\boldsymbol{x}/\|\boldsymbol{x}\|)\boldsymbol{Q}^{lk}_{Jm}, \tag{12}$$

where $\boldsymbol{Q}^{lk}_{Jm}$ are the Clebsch-Gordan matrices of shape $(2l+1)\times(2k+1)$, Y_{Jm} indicates the m's dimension of spherical harmonic $Y_J : \mathbb{R}^3 \to \mathbb{R}^{2J+1}$, and $\phi_J(\cdot)$ are learnable radial functions with input radial $\|\boldsymbol{x}\|$.

EGNN is a type of message passing graph neural networks with the equivariant graph convolutional layers (EGCL) defined on type-1 and type-0 features $(\boldsymbol{x}^{l+1}, \boldsymbol{h}^{l+1}) = \phi^l_{\text{EGNN}}(\boldsymbol{x}^l, \boldsymbol{h}^l)$, or formally as follows (l is the index of layer):

$$\begin{aligned} \boldsymbol{m}_{ij} &= \phi_m(\boldsymbol{h}^l_i, \boldsymbol{h}^l_j, d^2_{ij}, e_{ij}), \quad \boldsymbol{h}^{l+1}_i = \phi_h(\boldsymbol{h}^l_i, \sum_{j\in\mathcal{N}_i} a_{ij}\boldsymbol{m}_{ij}), \\ \boldsymbol{x}^{l+1}_i &= \boldsymbol{x}^l_i + \sum_{j\in\mathcal{N}_i}(\frac{\boldsymbol{x}^l_i - \boldsymbol{x}^l_j}{d_{ij}+1})\phi_x(\boldsymbol{h}^l_i, \boldsymbol{h}^l_j, d^2_{ij}, e_{ij}), \end{aligned} \tag{13}$$

where $d_{ij} := \|\boldsymbol{x}^l_i - \boldsymbol{x}^l_j\|_2$ denotes the Euclidean distance between two nodes w.r.t. their type-1 features, e_{ij} is the edge attributes from input, $a_{ij} = \phi_a(\boldsymbol{m}_{ij})$ indicates the attention mechanism that aggregates the message $\boldsymbol{m}_{ij}$, $\mathcal{N}_i$ is the neighborhood of node i, and the learnable mappings $(\phi_m, \phi_h, \phi_x, \phi_a)$ are parameterized by multi-layer perceptrons (MLP). The whole EGNN architecture is composed of L such layers to perform the non-linear and equivariant transformation.

Denoting the SE(3) convolutional layer as $\varphi_\theta(\cdot)$ and the EGNN network as $\text{EGNN}_\theta(\cdot)$, the equivariant score network used in our work has the composition form as $\mathbf{s}_\theta(\boldsymbol{x}, t) = \text{Out}^{(1)}\left[(\text{EGNN}_\theta \circ \varphi_\theta)(\boldsymbol{x}, \boldsymbol{h}^0(t))\right]$, where $\circ$ means the composition of two functions, $\text{Out}^{(1)}(\cdot)$ indicates extracting only the type-1 feature (vector field), $\boldsymbol{x}$ is the atom coordinates and $\boldsymbol{h}^0(t)$ is the time-dependent initial embedding (type-0 features). Since the special Euclidean group SE(3) is just a subgroup of the Euclidean group E(3) by excluding reflections, it is trivial to prove that the score network $\mathbf{s}_\theta(\mathbf{x}, t)$, composed of SE(3) and E(3)-equivariant functions, is SE(3)-equivariant w.r.t. $\mathbf{x}$ for any fixed t.

A.2. Implementation details

For equivariant score network, the nodes $\boldsymbol{x}^0$ (type-1) are initialized by the coordinates of the Cα atoms of the input conformation, while the node features $\boldsymbol{h}^0$ (type-0) are initialized by the sinusoidal time embedding and positional embedding (Vaswani et al., 2017). To be specific, both embeddings having a dimension of 128 are concatenated and then passed through a affine transformation and a followed layer normalization. The size of node embedding is 128 and we do not consider edge feature to construct the denoising network. The whole EGNN network consists of 4 convolutional layers, 128 features per layer and SiLU activation functions. The score network is trained for a total 10,000,000 updates with batch size 2, learning rate 1e-5 using Adam optimizer and a warmup linear schedule, where learning rate are linearly increasing to the maximum value for the first 100,000 steps and linearly decreasing to zero for the rest of steps. The training was deployed on NVIDIA Tesla V100-SXM2 32GB and the training process approximately lasted 24 GPU days for a single run. To determine the best model checkpoint for sampling experiments, we employed early stopping strategy to avoid overfitting based on the validation loss per epoch. For diffusion, we used $T = 1000$ as the total number of time steps. During sampling, the reverse diffusion samplers (Song et al., 2020) were adopted to discretize the reverse-time domain and calculate the integral.

A.3. Data processing

Following (Jing et al., 2023), we set the training split as all structures released before April 30th, 2020 while the validation split as structures between May 1st, 2020 and November 30th, 2020. Single chain structures with sequence length between 20 and 256 were used. On top of these, we removed structures if they meet any of the criteria: (1) have missing atom or coordinates; or (2) contain residue discontinuity; or (3) resolution >5Å. We also dropped out structures appearing in our evaluation benchmarks to prevent data leakage. Finally, we obtained a training set with 193,145 structures, plus a validation set containing 12,110 structures.

For each atom coordinate in the PDB dataset, we perform the whitening transformation by deducting a mean vector and element-wise rescaling by a factor. Specifically, for any protein conformation with N atoms $\mathbf{x} = (x_1, x_2, \dots, x_N)$, we apply $x_i \leftarrow (1/\hat{\sigma}_{\text{train}}) \odot (x_i - 1/N \sum_i x_i), \forall i$, where $x_i \in \mathbb{R}^3$ is the Euclidean coordinate (xyz) of the ith atom, $\hat{\sigma}_{\text{train}}$ is the standard deviation vector calculated independently for each component in 3D space (we denote as $x[0], x[1], x[2]$) among all the atom coordinates in the training set, while $\odot$ is Hadamard (element-wise) product operation. In practice, we set $\hat{\sigma}_{\text{train}}$=[10.08, 10.05, 10.74] and such statistic is computed from the whole training set.

A.4. Details of temperature-controlled sampling

Consider some probability distribution $p(\mathbf{x})$ to which we do not have access. We have done approximating its corresponding score function $\nabla_{\mathbf{x}} \log p_t(\mathbf{x})$ using a pre-trained network $\mathbf{s}_\theta(\mathbf{x}, t)$. Our goal is to find the $\beta-$tempering version of the score $\nabla_{\mathbf{x}} \log p_t^{(\beta)}(\mathbf{x})$ such that the backward SDE can be mediated by β. To derive its expression, we firstly consider the case of Gaussian data distribution, i.e., $\mathbf{x} \sim \mathcal{N}(\boldsymbol{\mu}_0, \boldsymbol{\Sigma}_0)$, and introduce the following lemma:

Lemma A.1. *Let $\mathbf{x}(0) \sim \mathcal{N}(\boldsymbol{\mu}_0, \boldsymbol{\Sigma}_0)$ be the data sample from some gaussian distribution, then the marginal distribution of perturbed data $\mathbf{x}(t)$ of Eq. (3) and (4) is subject to the following gaussian process:*

$$\mathbf{x}^{(VE)}(t) \sim \mathcal{N}(\mathbf{x}(t)|\boldsymbol{\mu}_0, \boldsymbol{\Sigma}_0 + (\sigma^2(t) - \sigma^2(0))\mathbf{I}), \tag{14}$$

and

$$\mathbf{x}^{(VP)}(t) \sim \mathcal{N}(\mathbf{x}(t)|\alpha(t)\boldsymbol{\mu}_0, \alpha^2(t)\boldsymbol{\Sigma}_0 + (1 - \alpha(t))^2\mathbf{I}), \tag{15}$$

where $\alpha(t) = \exp(-\frac{1}{2}\int_0^t \beta(s)ds)$. Then we can obtain the following score rescaling theorem:

Theorem A.2. *(Score rescaling) Suppose $\mathbf{x}(0) \in \mathbb{R}^d$ is Gaussian distributed with covariance matrix $\boldsymbol{\Sigma}$, then sampling via the backward process Eq. (2) with temperature control suffices to apply a linear transformation per time the score function at time t, or as the following form:*

$$\nabla_{\mathbf{x}} \log p_t^{(\beta)}(\mathbf{x}) = \mathbf{R}(t; \boldsymbol{\Sigma}, \beta)\nabla_{\mathbf{x}} \log p_t(\mathbf{x}), \tag{16}$$

where $\mathbf{R}(t;\boldsymbol{\Sigma},\beta) \in \mathbb{R}^{d\times d}$ is a time-dependent positive semi-definite matrix describing the tempering transformation, which only depends the covariance of data $\mathbf{x}(0)$ as well as an inverse temperature scalar $\beta > 0$. Especially, $\mathbf{R}(t;\boldsymbol{\Sigma},\beta = 1) \equiv \mathbf{I}$, i.e., sampling without tempering effect. See appendix for detailed proof of Lemma A.1 and Theorem A.2, along with their specific forms for different SDEs. The score rescaling in Eq. (16) only assumes Gaussian, yet this assumption can already be too strong. In the following section, we show that even when the Gaussian assumption fails to be made, we can still trade-off sample quality and diversity with the rescaling transformation via Eq. (16).

A.4.1. Proof of Lemma A.1

Below we give a detailed proof of A.1. Consider we have a data sample $\mathbf{x}_0 \in \mathbb{R}^d$ is normally distributed, then its marginal distribution is:

$$p_0(\mathbf{x}_0) = \mathcal{N}(\mathbf{x}_0|\boldsymbol{\mu}_0,\boldsymbol{\Sigma}_0) = \frac{1}{(2\pi)^{d/2}|\boldsymbol{\Sigma}|^{1/2}} \exp\left(-\frac{1}{2}(\mathbf{x}_0-\boldsymbol{\mu}_0)^T{\boldsymbol{\Sigma}_0}^{-1}(\mathbf{x}_0-\boldsymbol{\mu}_0)\right). \tag{17}$$

Because we need to derive both marginal distribution for both VESDE and VPSDE, we start with a more general case. Consider another conditional Gaussian distribution p_t for $\mathbf{x}_t$ given $\mathbf{x}_0$ in the form:

$$p_{t|0}(\mathbf{x}_t|\mathbf{x}_0) = \mathcal{N}(\mathbf{x}_t|\mathbf{A}\mathbf{x}_0 + \mathbf{b}, \boldsymbol{\Sigma}_t), \tag{18}$$

where $\mathbf{A} \in \mathbb{R}^{d\times d}, \mathbf{b} \in \mathbb{R}^d$ are parameters defining the linear function of its condition variable $\mathbf{x}_0$, and $\boldsymbol{\Sigma}_t$ is the covariance matrix of $\mathbf{x}_t$. This is exactly an example of a linear Gaussian model (Roweis & Ghahramani, 1999).

The derivation of $p_t(\mathbf{x}_t)$ involves computing the integral $\int_{\mathbf{x}} p_0(\mathbf{x})p_{t|0}(\mathbf{x}_t|\mathbf{x})d\mathbf{x}$, which in general can be as intractable as the evidence (normalizing constant of posterior) that appears in Bayesian inference. However, this can be solved in closed-form for Gaussian distributions. As proved in the Section 2.3.3 of (Bishop & Nasrabadi, 2006), the marginal distribution $p_t(\mathbf{x}_t)$ is also normally distributed and take the following form:

$$p_t(\mathbf{x}_t) = \mathcal{N}(\mathbf{x}_t|\mathbf{A}\boldsymbol{\mu}_0 + \mathbf{b}, \boldsymbol{\Sigma}_t + \mathbf{A}\boldsymbol{\Sigma}_0\mathbf{A}^\top), \tag{19}$$

Therefore, for VESDE, the perturbation kernel in Eq. (3) give the conditional distribution (Song et al., 2020) as:

$$p_{t|0}^{(\text{VE})}(\mathbf{x}_t|\mathbf{x}_0) = \mathcal{N}(\mathbf{x}_t|\mathbf{x}_0, (\sigma^2(t) - \sigma^2(0))\mathbf{I}), \tag{20}$$

where $\sigma(t)$ is noise scale function of VESDE and $t \in [0, T]$ is the continuous time variable. Then, plug in the conditional distribution back to Eq. (19), it finally yields

$$p_t^{(\text{VE})}(\mathbf{x}_t) = \mathcal{N}(\mathbf{x}_t|\boldsymbol{\mu}_0, \boldsymbol{\Sigma}_0 + (\sigma^2(t) - \sigma^2(0))\mathbf{I}). \tag{21}$$

Also, for VPSDE, the conditional distribution based on the perturbation kernel is:

$$p_{t|0}^{(\text{VP})}(\mathbf{x}_t|\mathbf{x}_0) = \mathcal{N}(\mathbf{x}_t|\alpha(t)\mathbf{x}_0, (1 - \alpha^2(t))\mathbf{I}), \tag{22}$$

where $\alpha(t) = \exp(-\frac{1}{2}\int_0^t \beta(s)ds)$ and $\beta(t)$ is the noise function in VPSDE. Similar to above, the marginal distribution of $\mathbf{x}_t$ is:

$$p_t^{(\text{VP})}(\mathbf{x}_t) = \mathcal{N}(\mathbf{x}_t|\alpha(t)\boldsymbol{\mu}_0, \alpha^2(t)\boldsymbol{\Sigma}_0 + (1 - \alpha^2(t))\mathbf{I}), \tag{23}$$

A.4.2. Proof of Theorem A.2

Since we have obtained the marginal distributions $p_t(\mathbf{x}_t)$ as above, we can prove the Theorem A.2 by giving the specific form of tempering transformation. Consider the general form of marginal distribution as 19, based on the density function of Gaussian distribution, the corresponding score function can be written as:

$$\nabla_{\mathbf{x}_t} \log p_t(\mathbf{x}_t) = -(\mathbf{\Sigma}_t + \mathbf{A}\mathbf{\Sigma}_0\mathbf{A}^\top)^{-1} (\mathbf{x}_t - (\mathbf{A}\boldsymbol{\mu}_0 + \mathbf{b})), \tag{24}$$

Now suppose we want to "temper" the original data distribution $p_0(\mathbf{x}_0) = \mathcal{N}(\mathbf{x}_0|\boldsymbol{\mu}_0, \mathbf{\Sigma}_0)$ to a inverse temperature factor $\beta > 0$, i.e.,

$$p_0^{(\beta)}(\mathbf{x}_0) = \frac{(p_0(\mathbf{x}_0))^\beta}{Z_\beta} = \mathcal{N}(\mathbf{x}_0|\boldsymbol{\mu}_0, \beta^{-1}\mathbf{\Sigma}_0), \tag{25}$$

where Z_β is the normalizing constant. This indicates the inverse temperature β actually rescales the data covariance by a factor $1/\beta$. Plug-in back to Eq. (24), we have:

$$\begin{aligned}\nabla_{\mathbf{x}_t} \log^{(\beta)} p_t(\mathbf{x}_t) &= -(\mathbf{\Sigma}_t + \beta^{-1}\mathbf{A}\mathbf{\Sigma}_0\mathbf{A}^\top)^{-1} (\mathbf{x}_t - (\mathbf{A}\boldsymbol{\mu}_0 + \mathbf{b}))\\ &= -(\mathbf{\Sigma}_t + \beta^{-1}\mathbf{A}\mathbf{\Sigma}_0\mathbf{A}^\top)^{-1} \left[(\mathbf{\Sigma}_t + \mathbf{A}\mathbf{\Sigma}_0\mathbf{A}^\top)(\mathbf{\Sigma}_t + \mathbf{A}\mathbf{\Sigma}_0\mathbf{A}^\top)^{-1}\right] (\mathbf{x}_t - (\mathbf{A}\boldsymbol{\mu}_0 + \mathbf{b}))\\ &= (\mathbf{\Sigma}_t + \beta^{-1}\mathbf{A}\mathbf{\Sigma}_0\mathbf{A}^\top)^{-1}(\mathbf{\Sigma}_t + \mathbf{A}\mathbf{\Sigma}_0\mathbf{A}^\top) \left[-(\mathbf{\Sigma}_t + \mathbf{A}\mathbf{\Sigma}_0\mathbf{A}^\top)^{-1} (\mathbf{x}_t - (\mathbf{A}\boldsymbol{\mu}_0 + \mathbf{b}))\right]\\ &= (\mathbf{\Sigma}_t + \beta^{-1}\mathbf{A}\mathbf{\Sigma}_0\mathbf{A}^\top)^{-1}(\mathbf{\Sigma}_t + \mathbf{A}\mathbf{\Sigma}_0\mathbf{A}^\top)\nabla_{\mathbf{x}_t} \log p_t(\mathbf{x}_t).\end{aligned} \tag{26}$$

Finally, let $\mathbf{R}(t;\mathbf{\Sigma},\beta) \coloneqq (\mathbf{\Sigma}_t + \beta^{-1}\mathbf{A}\mathbf{\Sigma}_0\mathbf{A}^\top)^{-1}(\mathbf{\Sigma}_t + \mathbf{A}\mathbf{\Sigma}_0\mathbf{A}^\top)$, we have the result of Theorem A.2:

$$\nabla_{\mathbf{x}} \log p_t^{(\beta)}(\mathbf{x}) = \mathbf{R}(t;\mathbf{\Sigma},\beta)\nabla_{\mathbf{x}} \log p_t(\mathbf{x}). \tag{27}$$

Note that for different SDEs, the tempering transformation $\mathbf{R}(t;\mathbf{\Sigma},\beta)$ takes different forms since it is also determined by $\mathbf{\Sigma}_t$ and $\mathbf{A}$, which are further determined by the noise schedule functions. To be specific, for VESDE, $\mathbf{A} = \mathbf{I}, \mathbf{\Sigma}_t = (\sigma^2(t) - \sigma^2(0))\mathbf{I}$; for VPSDE, $\mathbf{A} = \alpha(t)\mathbf{I}, \mathbf{\Sigma}_t = (1 - \alpha^2(t))\mathbf{I}$. Therefore, by plugging in, the tempering transformation will be:

$$\mathbf{R}^{(\text{VE})}(t;\mathbf{\Sigma},\beta) \coloneqq ((\sigma^2(t) - \sigma^2(0))\mathbf{I} + \frac{1}{\beta}\mathbf{\Sigma}_0)^{-1}((\sigma^2(t) - \sigma^2(0))\mathbf{I} + \mathbf{\Sigma}_0), \tag{28}$$

for VESDE and

$$\mathbf{R}^{(\text{VP})}(t;\mathbf{\Sigma},\beta) \coloneqq ((1 - \alpha^2(t))\mathbf{I} + \frac{\alpha^2(t)}{\beta}\mathbf{\Sigma}_0)^{-1}((1 - \alpha^2(t))\mathbf{I} + \alpha^2(t)\mathbf{\Sigma}_0), \tag{29}$$

for VPSDE.

A.4.3. Covariance determination

According to Eq. (16), we need to compute the covariance matrix $\mathbf{\Sigma}$ in order to properly rescale the score function during sampling. Because covariance $\mathbf{\Sigma}$ for the test protein in benchmark set cannot assume to be accessible during inference, we estimate it using the covariance of training set $\mathbf{\Sigma} \approx \hat{\mathbf{\Sigma}}_{\text{train}}$ since they can be viewed as identically distributed. To accommodate structures with different length, we adopt a simple strategy by applying the unified covariance matrix for each atom and concatenate together, such that $\mathbf{\Sigma}$ has the following block diagonal form:

$$\begin{bmatrix}\mathbf{\Sigma}_{\text{a}} & \mathbf{0} & \dots & \mathbf{0}\\ \mathbf{0} & \mathbf{\Sigma}_{\text{a}} & \dots & \mathbf{0}\\ \vdots & \vdots & \vdots & \vdots\\ \mathbf{0} & \dots & \mathbf{0} & \mathbf{\Sigma}_{\text{a}}\end{bmatrix}$$

where $\mathbf{\Sigma}_{\text{a}} \in \mathbb{R}^{3\times 3}$ is the covariance matrix calculated among all the atoms in the training set, and the number of blocks in a row or column depends on the number of atoms in the test protein when applying the rescaling transformation. We then

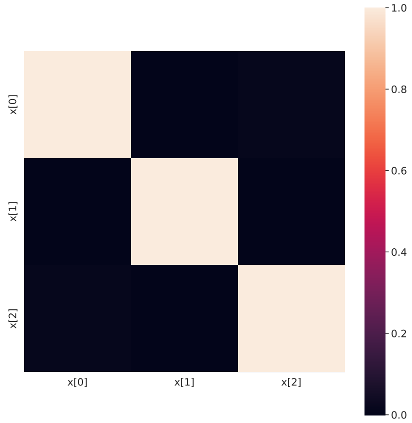

Figure S1. Covariance matrix $\mathbf{\Sigma}_{\text{a}}$ calculated among all atom coordinates in the training set after the whitening process as in A.3.

evaluate $\mathbf{\Sigma}_{\text{train}}$ for the training net after whitening. As shown in Fig. S1, the $\mathbf{\Sigma}_{\text{a}}$ is nearly a identity matrix in $\mathbb{R}^3$ and thus the $\mathbf{\Sigma}$ can be as simple as a identity matrix in $\mathbb{R}^{N\times 3}$ when applying to a protein with N atoms.

A.5. Pseudo free energy computation

Similar to the likelihood computation in probability flow ODE (Song et al., 2020), we can also derive from Eq. (8) the (pseudo) free energy with the pretrained score functions. This can be used for energy reweighting (Noé et al., 2019) of the sampled ensemble to Boltzmann distribution, which is useful for computing thermodynamics quantities. We firstly write the probability flow ODE that belongs to the backward diffusion in Eq. (2) by replacing the score function with time-conditioned score network $\mathbf{s}_\theta(\mathbf{x},t)$ as follows (negative dt, same below):

$$d\mathbf{x} = [\mathbf{f}(\mathbf{x},t) - \frac{1}{2}g^2(t)\nabla_{\mathbf{x}}\mathbf{s}_\theta(\mathbf{x},t)]dt. \tag{30}$$

Let $\tilde{\mathbf{f}}_\theta(\mathbf{x},t) := \mathbf{f}(\mathbf{x},t) - \frac{1}{2}g^2(t)\nabla_{\mathbf{x}}\mathbf{s}_\theta(\mathbf{x},t)$, and consider a sampled conformation $\tilde{\mathbf{x}}$ from input conformation $\mathbf{x}(0)$, we can compute the pseudo free energy (PFE) by employing the instantaneous change of variables formula (Chen et al., 2018):

$$\text{PFE}(\tilde{\mathbf{x}}_0) = -\log p_{\delta T|0}(\mathbf{x}(\delta T)|\mathbf{x}(0)) - \int_0^{\delta T} \nabla\cdot\tilde{\mathbf{f}}_\theta(\mathbf{x}(t),t)dt, \tag{31}$$

where the perturbed sample $\mathbf{x}(\delta T)$ and $\log p_{\delta T|0}(\mathbf{x}(\delta T)|\mathbf{x}(0))$ are explicitly defined by the perturbation kernel in Eq. (6) and can be evaluated in closed-form. To reduce the expensive computation of the second term, we may used the Skilling-Hutchinson trace estimator (Hutchinson, 1989; Skilling, 1989) as suggested in (Grathwohl et al., 2018; Song et al., 2020):

$$\nabla\cdot\tilde{\mathbf{f}}_\theta(\mathbf{x},t) = \mathbb{E}_{p(\epsilon)}[\epsilon^\top\nabla\tilde{\mathbf{f}}_\theta(\mathbf{x},t)\epsilon], \tag{32}$$

where $\nabla\tilde{\mathbf{f}}_\theta(\mathbf{x},t)$ denotes the Jacobian of $\tilde{\mathbf{f}}_\theta(\cdot,t)$, and the $\epsilon\in\mathbb{R}^d$ is a white noise, i.e., $\mathbb{E}[\epsilon]=\mathbf{0}$ and $\text{Cov}[\epsilon]=\mathbf{I}$. In practice, we can sample $\epsilon\sim p(\epsilon)$ and compute the unbiased estimation using above equation up to arbitrarily small error (Song et al., 2020) given sufficient computation.

A.6. Pseudocode of forward-backward dynamics

The pseudocode for the forward-backward dynamics is shown in Algorithm 1 and 2 for better illustration.

Algorithm 1 Forward-backward dynamics (VESDE)

```
Require: input conformation $\mathbf{x}$, constant perturbation scale $\delta$; time upper bound for diffusion process $T$; score network $\mathbf{s}_\theta$; noise scale function $\sigma$; data covariance $\mathbf{\Sigma}$; inverse temperature $\tau$.
$\mathbf{x}_0 \leftarrow \mathbf{x}$    // initialize state
$\{t_1, \dots, t_M\} \leftarrow$ Discretize($[0, \delta T]$)    // discretize time domain
for $i = 1$ to $M$ do
    $\mathbf{z} \sim \mathcal{N}(\mathbf{0}, \mathbf{I})$
    $\mathbf{x}_i \leftarrow \mathbf{x}_{i-1} + \sqrt{\sigma^2(t_i) - \sigma^2(t_{i-1})}\mathbf{z}$
for $i = M - 1$ to $0$ do
    $\mathbf{R}_{i+1} \leftarrow \mathbf{R}(t_{i+1}; \mathbf{\Sigma}, \tau)$    // in Eq. (28)
    $\mathbf{s}'_{i+1} \leftarrow \mathbf{R}_{i+1}\mathbf{s}_\theta(\mathbf{x}_{i+1}, \sigma(t_{i+1}))$    // score rescaling
    $\mathbf{x}'_i \leftarrow \mathbf{x}_{i+1} + \left[\sigma^2(t_{i+1}) - \sigma^2(t_i)\right] \mathbf{s}'_{i+1}$
    $\mathbf{z} \sim \mathcal{N}(\mathbf{0}, \mathbf{I})$
    $\mathbf{x}_i \leftarrow \mathbf{x}'_i + \sqrt{\sigma^2(t_{i+1}) - \sigma^2(t_i)}\mathbf{z}$
return $\mathbf{x}_0$
```

Algorithm 2 Forward-backward dynamics (VPSDE)

```
Require: input conformation $\mathbf{x}$, constant perturbation scale $\delta$; time upper bound for diffusion process $T$; score network $\mathbf{s}_\theta$; noise scale function $\beta$; data covariance $\mathbf{\Sigma}$; inverse temperature $\tau$.
$\mathbf{x}_0 \leftarrow \mathbf{x}$    // initialize state
$\{t_1, \dots, t_M\} \leftarrow$ Discretize($[0, \delta T]$)    // discretize time domain
for $i = 1$ to $M$ do
    $\mathbf{z} \sim \mathcal{N}(\mathbf{0}, \mathbf{I})$
    $\mathbf{x}_i \leftarrow \sqrt{1 - \beta(t_i)}\mathbf{x}_{i-1} + \sqrt{\beta(t_i)}\mathbf{z}$
for $i = M - 1$ to $0$ do
    $\mathbf{R}_{i+1} \leftarrow \mathbf{R}(t_{i+1}; \mathbf{\Sigma}, \tau)$    // in Eq. (29)
    $\mathbf{s}'_{i+1} \leftarrow \mathbf{R}_{i+1}\mathbf{s}_\theta(\mathbf{x}_{i+1}, t_{i+1})$    // score rescaling
    $\mathbf{x}'_i \leftarrow \left[2 - \sqrt{1 - \beta(t_{i+1})}\right] \mathbf{x}_{i+1} + \beta(t_{i+1})\mathbf{s}'_{i+1}$
    $\mathbf{z} \sim \mathcal{N}(\mathbf{0}, \mathbf{I})$
    $\mathbf{x}_i \leftarrow \mathbf{x}'_i + \sqrt{\beta(t_{i+1})}\mathbf{z}$
return $\mathbf{x}_0$
```

B. Details of evaluation metrics

In this section, we elaborate the definition of the evaluation metrics introduced in the experiments.

Validity The Validity is defined as the ratio of clash conformations. It is calculated as the number of conformations that contain steric clashes divided by the number of all evaluating examples. Steric clash is determined by whether two contacting atoms is too close to each other. For an example conformational ensemble $\mathbf{X} \coloneqq \{\mathbf{x}_i\}_{i=1}^n$, we have:

$$\text{Validity}(\{\mathbf{x}_i\}_{i=1}^n) = 1 - \frac{1}{n}\sum_{i=1}^{n} \mathbf{1}\{\exists j, k,\ \text{s.t. } d(\mathbf{x}_i[j], \mathbf{x}_i[k]) < d_0 \text{ and } |j-k| > 2\}, \tag{33}$$

where $\mathbf{x}[j] \in \mathbb{R}^3$ indicates the coordinate of the j's atom in conformation $\mathbf{x}$, $d_0 > 0$ is the distance threshold to discriminate steric clash, and the contacting pairs are only considered to be those beyond the 2-hop neighborhood along the chain ($|j-k| > 2$). In practice, we choose d_0 according to the van der Waals radius of C_α (1.7Å) minus an allowable overlap δ_d, or formally $d_0 = 2 \times 1.7 - \delta_d$ (unit : Å). The default value of δ_d is set to be 0.4Å, which is a reasonable value when examining protein-protein interactions (Ramachandran et al., 2011).

Fidelity The fidelity of a set of conformations is evaluated by measuring the similarity between the distribution of the reference ensemble $\mathbf{X}$ and the distribution of generated ensemble $\tilde{\mathbf{X}}$, which takes the idea of Fréchet inception distance (FID) (Heusel et al., 2017) for the evaluation of image synthesis. Following (Janson et al., 2023), we adopt two distributions that can loyally reflect the ensemble characteristics: (1) pairwise distance distribution, a $N \times N \times C$ tensor $\boldsymbol{D}$ (N is the number of atoms of each conformation), whose element $\boldsymbol{D}[i,j] = (p_1^{(ij)}, \ldots, p_C^{(ij)})$ records the discretized distance distribution $p^{(ij)} = \text{Cat}(p_1^{(ij)}, \ldots, p_C^{(ij)})$ of a pair of atom i and j among conformations in ensemble. Following (Janson et al., 2023), the distance range between minimum and maximum values is equally divided by $C = 50$ bins to give the categorical distribution; (2) radius of gyration distribution, where similar discretization treatment is applied same as above. On top of these, the Jensen-Shannon (JS) divergences is applied for both distributions between the reference ensemble and generated ensemble due to its symmetric property. It takes the following form (D_{KL} denotes the Kullback–Leibler (KL) divergence, p, q are distribution):

$$D_{JS}(p \parallel q) = \frac{1}{2}D_{KL}(p \parallel m) + \frac{1}{2}D_{KL}(q \parallel m), \text{ where } m = \frac{1}{2}(p+q). \tag{34}$$

Note that there exists $N(N-1)/2$ pairs of atoms in a N-atom conformation. To derive a scalar divergence between two input ensembles, we use the averaged JS divergence (Janson et al., 2023) over all atom pairs, or formally:

$$D_{JS}^{\text{avg}}(\mathbf{X} \parallel \tilde{\mathbf{X}}) = \frac{2}{N(N-1)}\sum_{i=1}^{N}\sum_{j=i+1}^{N} D_{JS}(p^{(ij)} \parallel \tilde{p}^{(ij)}). \tag{35}$$

Since the distribution of radius of gyration is uni-dimensional, the JS divergence is applied as usual.

Diversity The diversity of the ensemble of interest can be derived from any structural similarity score by enumerating and averaging the pairwise scores between two members of that ensemble. Here we adopt two most commonly used scoring functions: root mean square deviation (RMSD) and TM-score (Zhang & Skolnick, 2004). RMSD reflects the deviation degree in length (here we use nanometer (nm) as the unit) and is thus unnormalized. TM-score, on the contrary, is a normalized score to evaluate the structural similarity between two input structures, ranging from 0 to 1 and unit-free. A higher TM-score indicates that two structures share more similarity. Given above, the diversity (Div) of an ensemble $\mathbf{X} \coloneqq \{\mathbf{x}_i\}_{i=1}^n$ is defined as follows:

$$\text{Div-RMSD}(\mathbf{X}) = \frac{2}{n(n-1)}\sum_{i=1}^{n}\sum_{j=i+1}^{n} \text{RMSD}(\mathbf{x}_i, \mathbf{x}_j), \tag{36}$$

and

$$\text{Div-TM}(\mathbf{X}) = \frac{2}{n(n-1)} \sum_{i=1}^{n} \sum_{j=i+1}^{n} \left(1 - \text{TM}(\mathbf{x}_i, \mathbf{x}_j)\right), \tag{37}$$

where we apply the inverse score $[1 - \text{TM}(\cdot, \cdot)]$ to express diversity (the higher score the more diverse) aligned with RMSD. During evaluation, both scores are calculated using the officially released binary from (Zhang & Skolnick, 2004).

C. Implementation of other methods

C.1. Introduction of baseline models

As for baselines, AlphaFold2 (AF2) (Jumper et al., 2021) is notably powerful for its highly accurate structure prediction for unseen proteins. However, several recent studies (Chakravarty & Porter, 2022; Saldaño et al., 2022; Vani et al., 2022; Wayment-Steele et al., 2022) have investigated its potential for conformational sampling, with their results underscoring the limitations in conformational diversity. In accordance with these studies, We use AF2 with either no MSA (sequence only) or reduced MSA (Chakravarty & Porter, 2022) as input, running all 5 models under multiple random seed to encourage diversity; idpGAN (Janson et al., 2023) is a recently reported conditional generative method based on generative adversarial networks (GAN). idpGAN is trained with plenty of simulation data of intrinsically disordered peptides (IDP) and can generalize to generate unseen protein dynamics; Like idpGAN, EigenFold (Jing et al., 2023) is a recently developed generative structure prediction model that employs harmonic diffusion that enables diversity while keeping good accuracy. Specifically, EigenFold was trained on general PDB database and use the pre-computed embeddings from OmegaFold (Wu et al., 2022b), which are different from idpGAN.

C.2. AlphaFold2 structure prediction

The AlphaFold2 (AF2) (Jumper et al., 2021) predictions rely on an AF2 variant ParaFold (Zhong et al., 2022), which exploits the CPU parallelism to accelerate the multiple sequence alignment (MSA) query during the feature preparation stage and keeps the rest intact. We adapted the original pipelines to exploit AlphaFold2's mechanisms for sampling protein conformations. The 12 fast-folding proteins and BPTI were processed using all five AlphaFold pTM models, enabling a broad capture of potential conformations to enhance the prediction accuracy. Two distinct input settings, *reducedMSA* and *noMSA*, were used; the former simplified the MSA input by limiting concurrent sequence alignments, while the latter omitted the MSA entirely and and replaced it with a single sequence. In both settings, structure templates were not included to enhance the diversity of sampled conformations. This protocol is inspired by the protocol of AlphaFold2-RAVE (Vani et al., 2023), which exploited the potential capacity of AlphaFold2 to generate many possible conformations.

Specifically, in the *reducedMSA* setting, JackHMMER and HHBlits were used for searching MSA from databases including UniRef90, MGnify, and BFD, following AlphaFold2's original pipeline (Jumper et al., 2021). Only a small portion of the found MSA was used as input to compute the MSA representation fed to Evoformer, consistent with the method in (Del Alamo et al., 2022; Vani et al., 2023), `'max_extra_msa'` and `'max_msa_clusters'` were set to be 16 and 8 respectively. Conversely, the *noMSA* setting created a dummy MSA file as precomputed MSA for AlphaFold2 and as a result only a single sequence is used to predict structure. For both settings, each pTM model was repeated 20 times with varying random seeds.

C.3. Full-atom molecular dynamics simulations

To compare SENS with traditional molecular dynamics methods, we employ OpenMM (version 8.0) (Eastman et al., 2017) to conduct short MD simulations on our fast-folding protein benchmark systems as well as BPTI. Initial structures were taken from long simulations of (Lindorff-Larsen et al., 2011) and (Shaw et al., 2010). AMBER ff14SB (Maier et al., 2015) was used as the protein force-field and TIP3P was used as solvent model. All systems were neutralized and solvated in the boxes of 10 Å. All bonds involving hydrogen atoms were constrained with the SHAKE algorithm (Ciccotti & Ryckaert, 1986; Ryckaert et al., 1977). The particle mesh Ewald (PME) algorithm (Darden et al., 1993) was used to calculate the long-range electrostatic interactions. Initial structures were relaxed with minimization until convergence, then subjected to the equilibration stage with 10 ps time step size in the NVT and NPT ensemble sequentially. The simulation temperature of each system was set according to the original paper (Lindorff-Larsen et al., 2011). Another independent simulation, with a 30K higher temperature under the same setting, was used for comparison, which we named `'high temp'`.

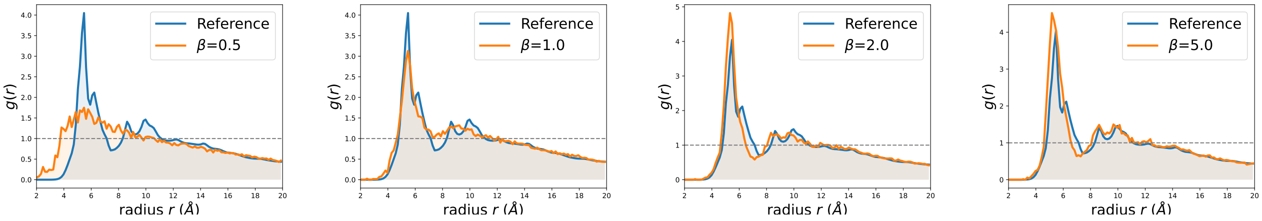

(a) $\beta = 0.5$ (b) $\beta = 1.0$ (c) $\beta = 2.0$ (d) $\beta = 5.0$

Figure S3. RDF of unconditionally sampled protein conformations, with Cα radius ranging from 2Å to 20Å. RDF of reference is colored as blue line while RDF of samples of specified β as orange line.

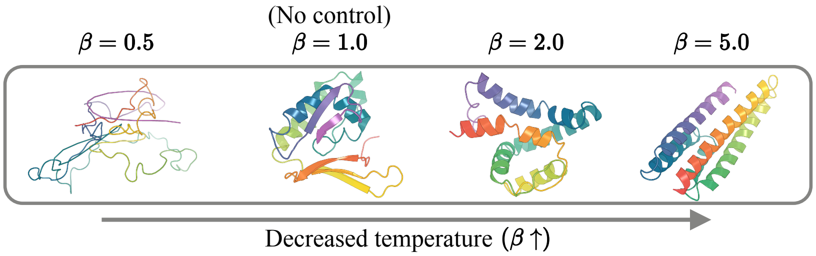

Figure S4. Visualization of protein examples unconditionally generated under different temperatures from noise. When temperature decreases (β increases), the structures exhibit an increased propensity for structural components.

D. Extended results

D.1. Unconditional sampling

In order to validate the proposed method, we firstly investigated the effect of inverse temperature β on the generative (backward) process. For evaluation, we generated 100 samples of length 128 from Gaussian noise under different β (ranging from 0.5 to 5.0) respectively. Note that when $\beta = 1.0$, sampling is not affected by temperature.

Firstly, we computed the radial distribution function (RDF) of Cα for the sampled conformations and reference set, which was curated from CATH v4.3 (Sillitoe et al., 2021) with 40% sequence identity since it represents a good structural coverage of protein space. As shown in Fig. S3, as the temperature decreases, the RDF of generated samples becomes similar to RDF of reference. Moreover, as shown in Fig. S2, the pairwise TM-score increases/RMSD decreases while we decrease the temperature for sampling, which low temperature can uniformly lead to less diverse sampled ensembles. Lastly, we visualized the generated protein ribbon under different temperatures in Fig. S4. It demonstrates that decreasing temperature gives rise to samples with more structural components (more protein-like than random point clouds). Especially, when $\beta = 5.0$, the generated example exhibits the helical-bundle feature which is similar to high-quality *de novo* designed miniproteins (Cao et al., 2020).

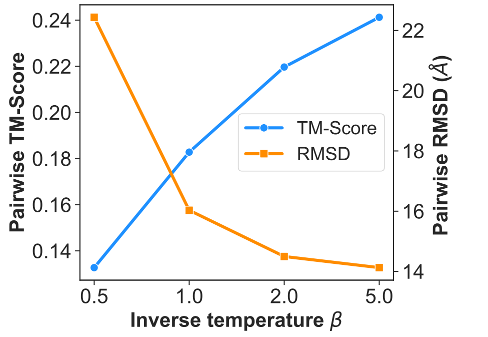

Figure S2. Pairwise TM-score (blue) and RMSD (orange) of unconditionally generated structures from SENS along with decreased temperature.

D.2. Per system pairwise distance and Rg distributions

In this section, we present the per system pairwise distance and radius of gyration distributions of all fast-folding protein systems, which are used to calculate the average fidelity scores shown in our main result. In Fig S5, the Rg distributions of selected methods are shown. In Fig. S6 and S7, the contacting probability distribution of different methods across all 12 benchmarking systems is shown, and each row indicates a specific protein

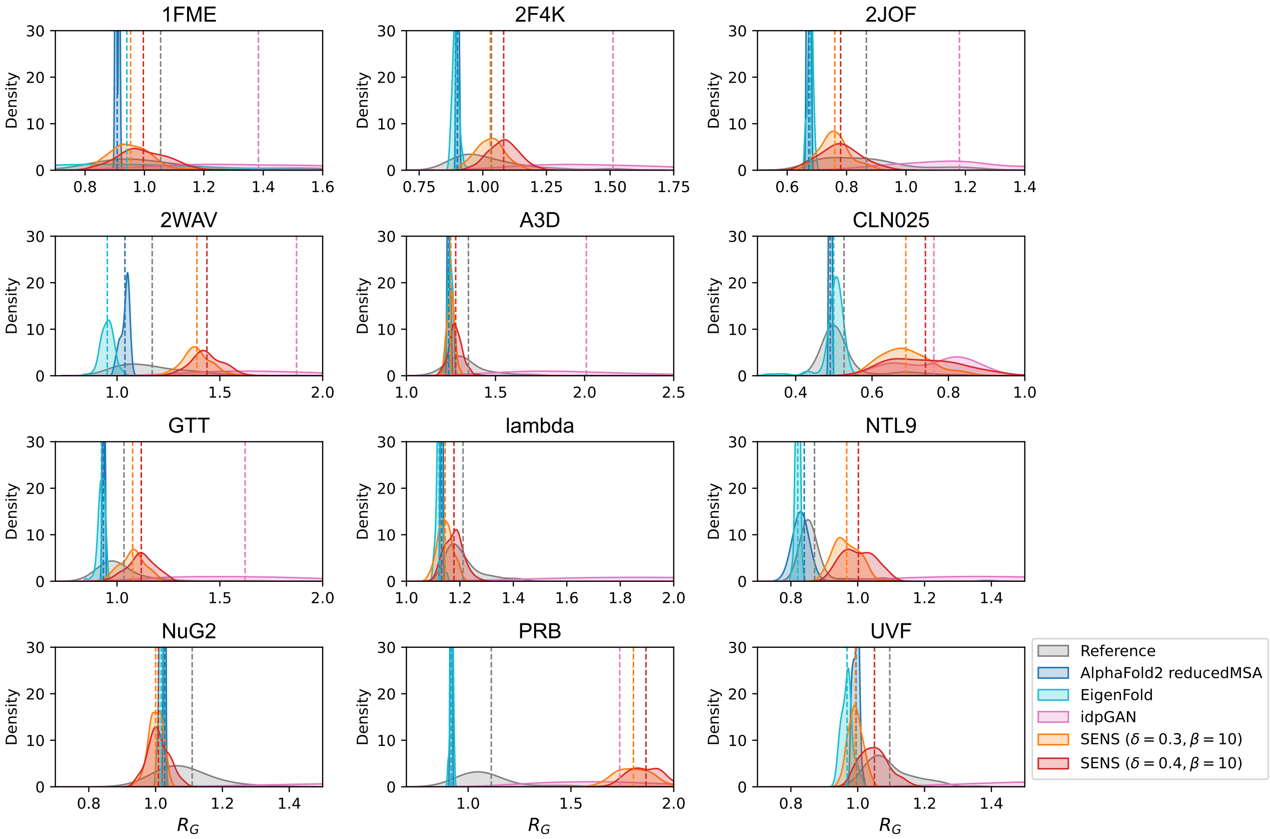

Figure S5. Rg distribution across all benchmarking systems. The shaded regions illustrate the spread of the Rg values for individual samples, while the dashed vertical lines mark the means of respective distributions.

system with the reference (full MD) result aligned in the rightmost column. The sampled conformations come from VESDE implementation of SENS as suggested in the main text.

D.3. More results for protein structural dynamics

We also tested the performance of SENS using VPSDE to construct the forward-backward dynamics proposed in the paper. The evaluation results under different hyperparameters are shown in Table S1, and are aligned with the VESDE counterpart. The results demonstrate that in general VPSDE can better capture the conformational distribution (lower JS divergence on average and higher diversity), yet cause more structural clashes (lower validity) in the sampled conformations. This scenario could result from the decaying drift term $-\frac{1}{2}\beta(t)\mathbf{x}$ in VPSDE and not in VESDE over-destroying the input structure during forward process. In particular, a β value of 5.0 can result in a temperature that is excessively low for VPSDE—though not for VESDE—impacting the generation of non-clashing conformations. In practice, one might need to carefully and heuristically tune the parameters δ, β for different systems and when using different diffusion dynamics to find the best value.

D.4. Apo/Holo conformational diversity

Following (Jing et al., 2023; Saldaño et al., 2022), we tested SENS with other non-MD baseline methods (AlphaFold2, idpGAN, EigenFold) on the apo/holo pairs of conformers (Saldaño et al., 2022). To accommodate the training protein lengths, we adopt a subset of 66 pairs with length less than or equal to 256 residues out of 91 structure pairs proposed in (Saldaño et al., 2022). For each target pair, a conformational ensemble of size 10 sampled from each model is tested. For evaluation, we adopted the same metric *TM_ens* defined in (Jing et al., 2023), which evaluates to what degree the resulting

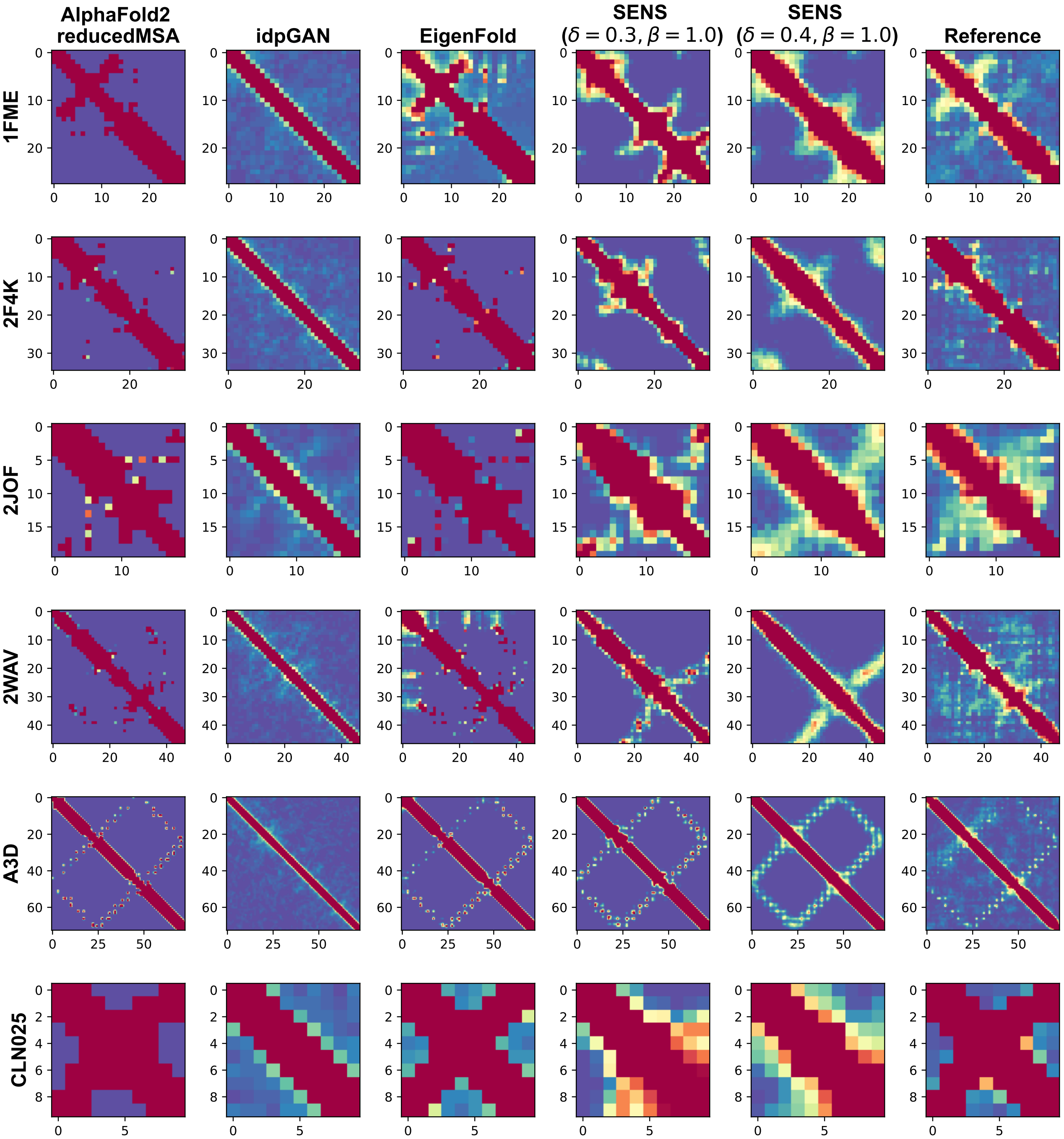

Figure S6. The contact probability distribution for all benchmarking systems. The color gradient illustrates the probability of contact, with red indicating a higher probability and blue a lower one. Contact is defined here as a Cα-Cα distance less than 8 Å.

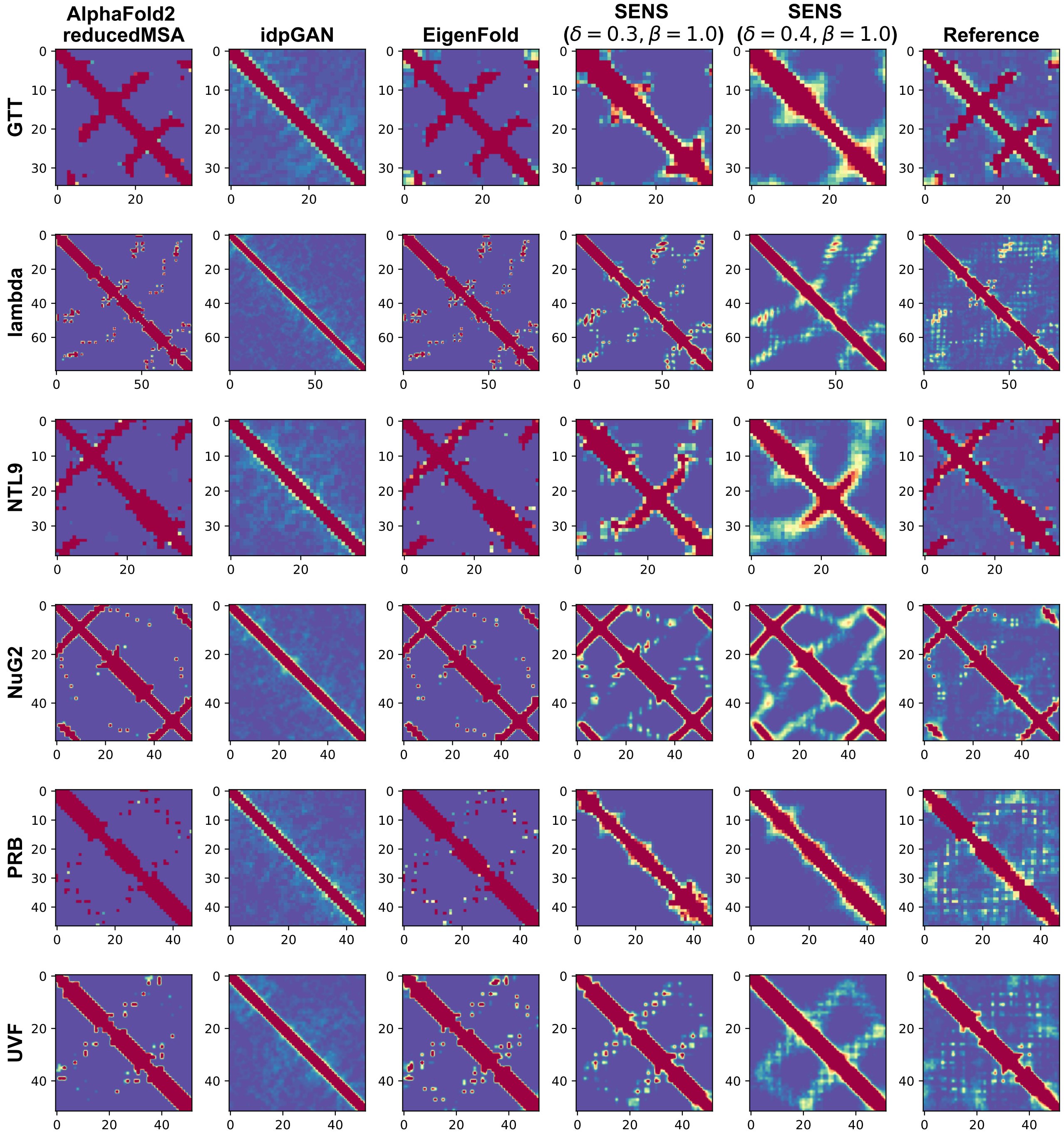

Figure S7. Extended part of Fig. S6.

Table S1. Benchmark results of VE/VPSDE under different hyperparameters. Best results among those using VESDE or VPSDE are **bolded**.

	Validity(↑)	JS-D(↓)	JS-Rg (↓)	Div-TM(↑)	Div-RMSD(↑)
VPSDE ($\delta = 0.3, \beta = 5.0$)	0.521	0.275	0.549	0.769	0.730
VPSDE ($\delta = 0.4, \beta = 5.0$)	0.553	0.280	0.589	0.774	0.787
VPSDE ($\delta = 0.3, \beta = 2.0$)	0.989	0.222	0.430	0.761	0.743
VPSDE ($\delta = 0.4, \beta = 2.0$)	0.990	0.224	0.468	0.767	0.827
VPSDE ($\delta = 0.3, \beta = 1.0$)	0.959	**0.186**	**0.296**	0.814	0.878
VPSDE ($\delta = 0.4, \beta = 1.0$)	0.958	0.193	0.321	**0.819**	**0.932**
VESDE ($\delta = 0.3, \beta = 5.0$)	**1.000**	0.283	0.524	0.543	0.275
VESDE ($\delta = 0.4, \beta = 5.0$)	**1.000**	0.252	0.422	0.647	0.401
VESDE ($\delta = 0.3, \beta = 2.0$)	**1.000**	0.267	0.474	0.536	0.277
VESDE ($\delta = 0.4, \beta = 2.0$)	0.998	0.217	0.401	0.693	0.440
VESDE ($\delta = 0.3, \beta = 1.0$)	0.998	0.257	0.416	0.576	0.295
VESDE ($\delta = 0.4, \beta = 1.0$)	0.993	0.203	0.338	0.734	0.498
Short MD 0.1μs	1.000	0.217	0.300	0.508	0.449
Short MD 0.1μs (high temp.)	1.000	0.204	0.285	0.536	0.495
Reference 1μs	1.000	0.135	0.178	0.582	0.642
Reference 10μs	1.000	0.100	0.156	0.650	0.736
Reference full	1.000	0.000	0.000	0.659	0.756

ensemble captures both the apo and holo states. By definition,

$$\mathrm{TM}_{\mathrm{ens}}(\mathbf{x}_{\mathrm{apo}}, \mathbf{x}_{\mathrm{holo}}, \{\mathbf{y}_i\}) = \frac{1}{2}\left[\max_i \mathrm{TM}(\mathbf{y}_i, \mathbf{x}_{\mathrm{apo}}) + \max_i \mathrm{TM}(\mathbf{y}_i, \mathbf{x}_{\mathrm{holo}})\right], \tag{38}$$

where $\mathbf{x}_{\mathrm{apo}}, \mathbf{x}_{\mathrm{holo}}$ denote the pair of ground truth apo/holo structures respectively, $\{\mathbf{y}_i\}$ indicates the generated ensemble. Similar to EigenFold, we plot the *TM_ens* scores for each apo/holo pair jointly with the intrinsic TM-score (calculated between apo/holo) denoted as *TM_conf1/2*. For baseline models, we input the protein sequence to obtain 10 different conformations; for SENS, we started with apo or holo structures and sampled 5 structures from either starting point.

As shown in Fig. S8, the results show that (generative) structure prediction models including AF2 and EigenFold can succeed in predicting only one form either apo or holo, and thus points are aggregated around the baseline result $y = 0.5x + 0.5$ (when the model can predict one single structure perfectly). Notably, when there is no MSA input, AF2 even failed to predict correctly single structure. For idpGAN, the generated ensembles show no relation with either apo or holo target such that the TM scores are all low. For the proposed SENS, since it had access to ground truth structure as starting point, the listed results demonstrate no improvements as well. As the δ increases, we find a declining TM_ens score, which indicates the sampled ensembles are isolated from both apo and holo forms. Among all these methods, not a single model achieves significant improvement over baseline on the apo/holo task, the solving of which can be important and interesting to serve as a future research direction.

E. Related works

Protein structure design A parallel research interest emerging recently focuses on the protein backbone structure design based on deep generative models. Early attempts include ProtDiff (Trippe et al., 2022), which generates novel CA-only backbones; protein structure-sequence co-generation based on structural constraints (Anand & Achim, 2022); and diffusion models tailored for antibody design (Luo et al., 2022). FoldingDiff complements these by applying diffusion to the dihedral angles of backbones. Chroma (Ingraham et al., 2022) designs novel protein backbones with several conditional inputs including natural language and comprehensively evaluates the programmability. Meanwhile, RFdiffusion (Watson et al., 2022) pushed the diffusion-based protein design to the experimental side and validated the effectiveness of generative modeling for this task. More advanced methods including Genie (Lin & AlQuraishi, 2023) and FrameDiff (Yim et al., 2023) have been proposed very recently, leveraging the invariant point attention (IPA) modules proposed by AF2 (Jumper et al., 2021) to enhance model capacity.

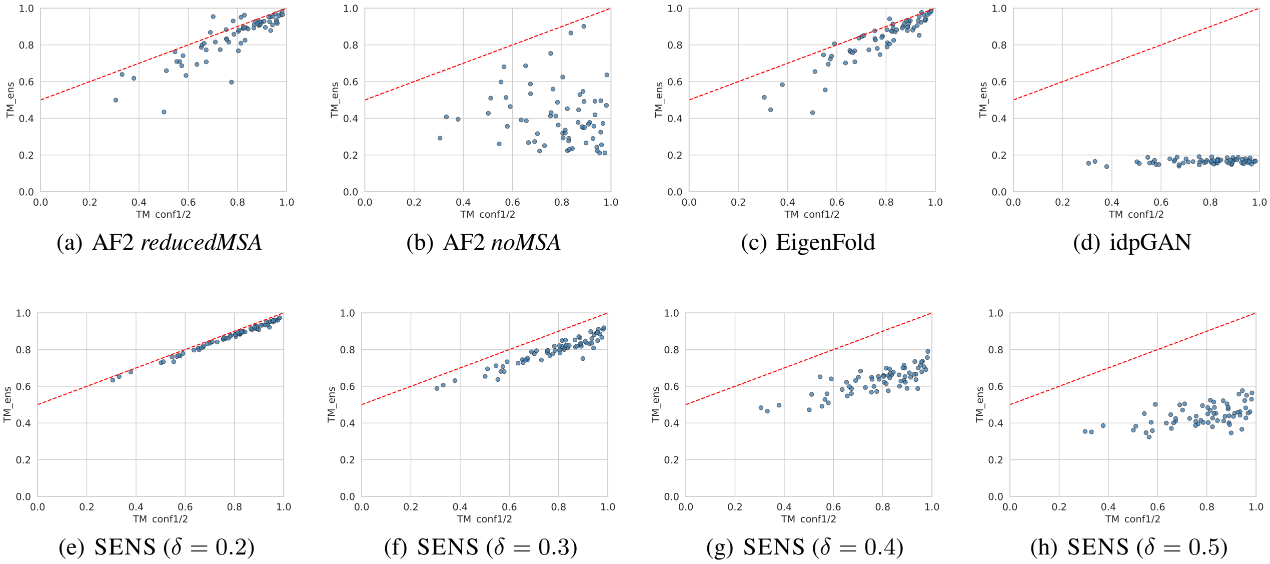

(a) AF2 *reducedMSA* (b) AF2 *noMSA* (c) EigenFold (d) idpGAN

(e) SENS ($\delta = 0.2$) (f) SENS ($\delta = 0.3$) (g) SENS ($\delta = 0.4$) (h) SENS ($\delta = 0.5$)

Figure S8. The scatter plots of TM_ens versus TM_conf1/2 on the apo/holo pairing dataset from different methods. The red line in each subfigure is the plot of $y = 0.5x + 0.5$ for a reference baseline.

Learning for protein dynamics Due to the inefficiency of classical simulations for protein dynamics (Bernardi et al., 2015; Karplus & McCammon, 2002), several works attempted to perform efficient sampling or learn neural force fields from simulation data. Boltzmann generators (Noé et al., 2019) were developed to generate equilibrium samples using normalizing flows (Dinh et al., 2014; Rezende & Mohamed, 2015) trained on simulation data or ground-truth energy. CGNets (Wang et al., 2019) proposed learning coarse-grained (CG) force fields trained by a force-matching objective in a supervised learning manner. Flow-matching (Kohler et al., 2023) improved this by complementing density estimation and sampling right before force-matching, thus not relying on ground-truth forces in simulation data. The most recent work (Arts et al., 2023) proposed to train diffusion model on samples from equilibrium distribution of a specific protein, and leveraged either the first-layer score function as learned force field or the entire backward diffusion to perform conformational sampling. However, these works can suffer from the transferability problem (Wang et al., 2019) and cannot be generalized to unseen proteins. While these methods were designed *ad hoc* and can only be applied to the proteins they are trained on, our method is distinguished from them by performing zero-shot conformation sampling, ready for modeling unseen protein dynamics.

F. Further discussion

In this paper, we have proposed the SENS for conformational sampling which leverages the bidirectional diffusion dynamics in SGMs. This method shares several aspects with (generative) structure prediction and protein backbone generation methods. Structure predictions, with representative methods AlphaFold2 (Jumper et al., 2021) and RoseTTAFold (Baek et al., 2021), aim to recover the stablest protein folding state from its sequence. In terms of evaluation, crystal structures are used as ground truth to assess accuracy within the classical regression framework. Those methods that can predict highly accurate folding structure and generalize to unseen proteins (even quite a bit different from training data) are encouraged and have a good potential to replace the experimental techniques such as X-ray diffraction and electron microscopy. The generative structure predictions, with the representative EigenFold (Jing et al., 2023), treat the protein folding task from discriminative prediction to conditional distribution learning, which shares the idea of DiffDock (Corso et al., 2022). The step of "go generative" has a benefit as gaining predictive robustness yet may suffer from making additional assumption (discussion on this topic belongs to the structured prediction problem (Belanger & McCallum, 2016) in machine learning domains). One key assumption by employing generative protein structure prediction is that there exists multiple stable conformations from one single amino-acid sequence, which is common and reasonable to protein structures. However, one of the biggest concerns is the lack of ground truth multi-state structure data that belongs to a single sequence. We believe in the significance of exploring such topic not only for better augmenting the current folding methods but also for the potential application to promote the study of protein dynamics. Methods for generating protein backbones, such as

ProtDiff (Trippe et al., 2022), aim to complement the known protein space with *de novo*-designed backbone structures by generative models. The novel backbones are usually fed to an inverse folding model, for example ProteinMPNN (Dauparas et al., 2022), to further obtain the specific protein sequences that can potentially fold to those backbones. Such backbone generative models (Ingraham et al., 2022; Trippe et al., 2022; Watson et al., 2022; Wu et al., 2022a; Yim et al., 2023) effectively model the protein structure space and do yield protein-like decoys. The functionality of such generated decoys remains to be validated in the *in vitro* assays and seldom computational metrics can give good evaluations. Therefore, it is also promising to investigate such computational evaluation for the generated protein backbones. Moreover, since the goal of backbone generation is only to model the marginal distribution of backbone structures alone, one interesting question to be investigated is whether we can "go further generative" than the generative structure prediction models by modeling the joint distribution of both protein structures and sequences, generating structure and sequence in parallel similar to the frameworks of (Anand & Achim, 2022; Luo et al., 2022; Shi et al., 2022). We consider the study of these as our potential future works.